University of California
Santa Barbara

Steering Natural Dynamics to Yield Energy Efficient, Stable, and Agile Legged Locomotion

A dissertation submitted in partial satisfaction
of the requirements for the degree

Doctor of Philosophy
in
Mechanical Engineering

by

Sebastian E. Sovero

Committee in charge:

Professor Katie Byl (Advisor), Chair
Professor Brad Paden (Committee Member)
Professor Igor Mezic (Committee Member)
Professor Joao Hespanha (Committee Member)

September 2016

The Dissertation of Sebastian E. Sovero is approved.

_____

Professor Brad Paden (Committee Member)

_____

Professor Igor Mezic (Committee Member)

_____

Professor Joao Hespanha (Committee Member)

_____

Professor Katie Byl (Advisor), Committee Chair

June 2016

Steering Natural Dynamics to Yield Energy Efficient, Stable, and Agile Legged

Locomotion

Copyright © 2016

by

Sebastian E. Sovero

Dedicated to my family, friends, and friendly strangers

Acknowledgements

First and foremost, I would like to thank Professor Katie Byl for supporting and mentoring me through my graduate career. She fostered my dream of developing the next generation of exoskeletons and matured my ability to conduct research. Without her support none of this work would have been possible. Also thank you to Professor Brad Paden, Professor Igor Mezic, and Professor Joao Hespanha for serving on my committee and giving valuable feedback. Additionally, thank you to my lab mates at UCSB, who created a positive open research environment.

Outside of UCSB, thank you to Tim Swift, who was extremely supportive of my research interests and goals at Otherlab. I am grateful that Otherlab has a drive to make the world a better place and helping others do the same. Thank you to the tireless Otherlab hardware team: Brenton Piercy, Giancarlo Nucci, Leanne Luce, Callum Lamb, and Phil Hopkins, whose perseverance and ingenuity made this research possible. Additionally, thank you to Collin Smith for working countless extra hours to collect our data, and keeping a cheerful spirit even when an unexpected indoor rainstorm destroyed our equipment. Additionally, thank you to Nicholas Cox and Kevin Kemper for the sound advice, technical insights, and hard work.

Finally, thank you to my family, who was always there to support me though the difficult and trying times of graduate school. And thank you to my friends who balanced my life with unimaginable adventures.

Curriculum Vitæ
Sebastian E. Sovero

Education

2016	Ph.D. in Mechanical Engineering, University of California, Santa Barbara.
2009	M.A. in Mechanical Engineering, University of California, Los Angeles.
2008	B.S. in Mechanical and Ocean Engineering, Massachusetts Institute of Technology.

Publications

Sebastian E. Sovero, Collin Smith, Tim Swift, Katie Byl. Design of Metabolically Beneficial Exoskeletons. Presented for 2015 International Conference on Intelligent Robots and Systems

Sebastian E. Sovero, Cenk Oguz Saglam and Katie Byl. Passive Frontal Plane Stabilization in 3D Walking. Presented for 2015 International Conference on Intelligent Robots and Systems

Sebastian E. Sovero, Cenk Oguz Saglam and Katie Byl. presentation "Discrete Methods for Dynamic Foot Placement" at International Symposium on Adaptive Motion of Animals and Machines 2015

K Byl, D Umphred, M Byl, B Stockhart, C Clayton, S Sovero, and N Byl. In Neurological Rehabilitation. "Integrating Technology into the Clinical Practice", pp. 1113-1172. Elsevier, 6th edition, 2013

Abstract

Steering Natural Dynamics to Yield Energy Efficient, Stable, and Agile Legged
Locomotion

by

Sebastian E. Sovero

We investigate how natural dynamics can yield stable, agile, and energy efficient robotic
systems. Firstly, we cover a design with a single passive rolling element to stabilize frontal
plane dynamics for a 3D biped walking across a range of forward velocities and/or step
lengths. We examine aspects of the non-linear dynamics that contribute to the energy ef-
ficiency and stability of the system through simulations. Secondly, we examine switching
controllers that allow for agile foothold selection in 5-link walkers. We leverage dy-
namic programming and discretization of the reachable space to walk across intermittent
footholds. We utilize our meshing techniques to quantify stability and agility of these
switching controllers. Finally, we provide experimental data on the effect of extra mass
and power on humans at a variety of locations and forward velocities. This allows robot
and exoskeleton designers to optimize for energy performance by understanding mass
placements and power densities required for high performing legged locomotion. Finally,
we present experimental data for an exoskeleton capable of assisting across running and
walking speeds.

Contents

0.1 Permissions and Attributions

The thesis contains material from the following publications:

1. ©2015 IEEE. Reprinted, with permission, from Sebastian E. Sovero, Cenk Oguz Saglam and Katie Byl. Passive Frontal Plane Stabilization in 3D Walking. *IEEE/RSJ International Conference on Intelligent Robots and Systems (IROS)*, 2015.

2. ©2016 IEEE. Reprinted, with permission, from Sebastian Sovero, Katie Byl, and Tim Swift. Theoretical Performance Limits for a High Specific-Power Ankle Exoskeleton Device.*International Symposium on Experimental Robotics (ISER)* 2016.

Chapter 1

Introduction
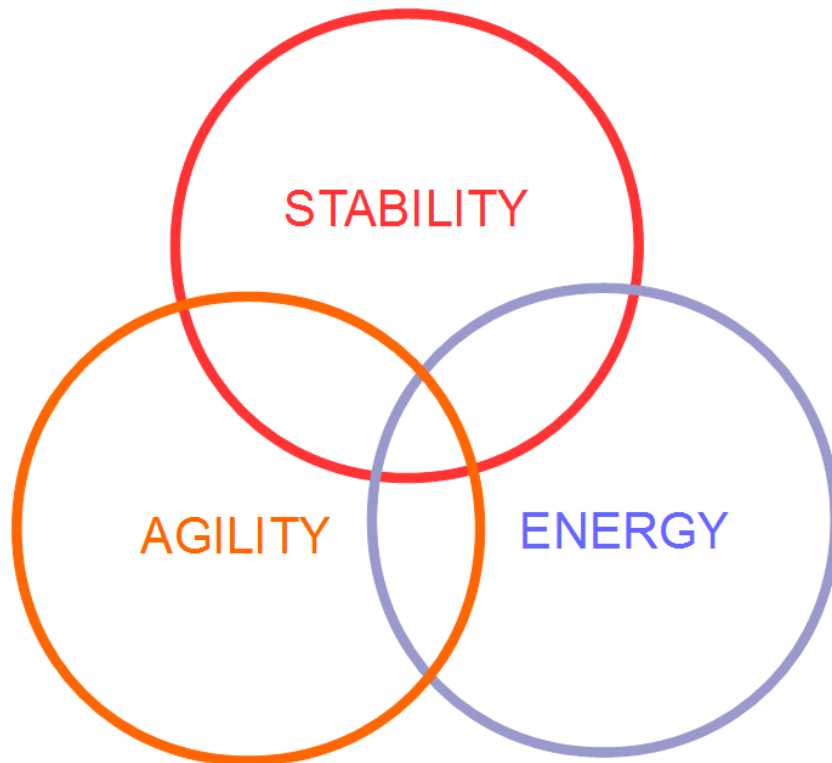
Figure 1.1: This Venn diagram represents the often conflicting goals that robot engineers attempt to achieve. There are trade-offs between stability, agility, and energy. Stability represents the ability of the system to reject unforeseen disturbances. Agility represents the ability of the robot to manipulate its dynamics to variability (limited footholds, obstacle avoidance, etc). Minimizing energy use is also important, since stored energy, such as batteries, adds weight and must be carried onboard for most practical mobile robot applications.

The field of legged robotics has been struggling to balance energy efficiency, agility, and stability. The energy efficiency of the robot directly affects how much energy is required for the robot to move around. A robot's agility definition varies among researchers, but here we take it to mean the ability of the robot to adapt to observed environmental or task demands. For example, if a robot visually detects that there are stepping obstacles, it can plan footholds in order to avoid those obstacles. Finally, achieving a classical notion of stability for a legged system has been possible for only restricted dynamic circumstances. The full nonlinear equations of motion, coupled with discrete impact dynamics, makes proving stability a difficult task. One approach among robotics engineers is to restrict the dynamics to provide more tractable systems, amenable to approximate analytic solutions, as the cost of likely sacrificing much of the performance potential of the robot. Chapters 2 and 3 discuss design and analysis techniques for improving both stability and agility, respectively, of biped robot models.

Finally, in Chapter 4 we transition to analysis of lower limb exoskeletons. In a field with similar but distinct dynamic challenges, engineers developing lower-limb, exoskeletons have been struggling with the same concerns and performance goals as legged robotic systems. For example, the energy consumption of the coupled robot/human system has broad implications for operating time and exhaustion levels of the human operator. The issue of stability is even more difficult for human/robot systems, as the human control system is poorly understood. Full knowledge of the control laws of the human are required to forward simulate the equations of dynamics. As the full equations of dynamics are generally necessary for stability analysis to be applied, this makes traditional tools inapplicable to exoskeleton systems. The agility of a exoskeleton can be quantified in terms of the type and variety of tasks that the human/robot system can accomplish together.

In Chapter 4, we present and describe experimental data to understand the effect

of mass and power on energetic locomotion costs to humans. While the primary goal of this work is to provide an optimization framework for exoskeleton designs, there are numerous scientific merits to this work. For example, if we understand the coupling between mass distribution and required power usage for a human, we also gain insight into how human anatomy, such as muscle size and placement, may naturally assist or hinder energy efficiency in biped walking.

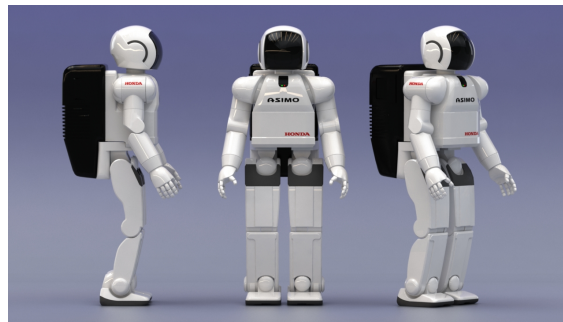## 1.1   Review of Legged Robot Design

Figure 1.2: The ASIMO robot is capable of walking and slow running with control.

Legged robotics offer the ability to traverse terrains that are impassable to more traditional wheeled robotics. Existing walking robots do not offer both efficiency and robustness to perturbations [3]. Zero moment point (ZMP) Robots such as Asimo (shown in Fig. 1.2), are able to carefully select their their footholds, but are not robust to sensing error. Most humanoid robots attempt to maintain direct control over all degrees of freedom by ensuring the center of pressure (CoP) always remains strictly within the support polygon of base of support, so that no tipping moments occur that would induce underactuated dynamics. Within the legged robotics community, center of pressure is commonly referred to as the ZPM of a system, since the center of pressure is also the point on the ground about which the net ground reaction force acts, i.e., about which

one can represent the reactive forces on the ground as a force vector, with no net moment imparted on the system from ground contact. Humanoid robots designed for ZMP control require a large number of degrees of freedom, to mimic the range of motion of a human, with high-torque actuators to control joint angles and correspondingly to set the zero-moment point accurately. They are designed to maintain a safety margin between the ZMP location on the ground and the edge of the base of support of the robot, which (on flat ground) is formed by the convex hull of all points of the robot that contact the ground; this provides a conservative criterion for stability. They are also designed to avoid operating near the kinematic limits of the robot, to allow for a range of motions when responding to unexpected perturbations while maintaining this ZMP criterion. As a result, such robots are dynamically constrained and cannot exploit the types of motions humans use during walking, in which the foot may act as a rolling contact, and tipping moments are actually exploited to propel forward walking.

One consequence of the more dynamic approach humans naturally use in walking is that humans provide an inspiration for better energetic efficiency. Energy use in locomotion for both machines and animals (including humans) is typically measured in terms of Cost of Transport (CoT). The CoT is a non-dimensional metric defined as the energy required to move a given distance divided by the change in potential energy of lifting the mass of that body the same distance upward under Earth's gravity field:

$$CoT \triangleq E/(mgd) = P/(mgv).$$

Human walking has a cost of transport of 0.05 [4], which is two orders of magnitude lower than a typical ZMP-based humanoid robot today. The advent of passive dynamic robots in the 1980s showed that exploiting the system's natural dynamics could yield stable walking cycles [2]. Active robots have been able to incorporate some of the energy

saving mechanism of passive dynamic walking robots. A recent example is the Cornell University Ranger robot, which demonstrated a cost of transport of 0.28 in 2010 [5]. While this is an impressive cost of transport for a robot, the robot was only able to walk in a roughly straight line and on flat terrain. The Cornell robot designers purposely chose energy optimization over agility. In order for legged robots to be practical, we need to lower the cost of transport of existing designs while still achieving enough stability for agility for practical applications.

Figure 1.3: This walking robot designed by Collins et al. [1] utilized passive dynamics for stabilization and locomotion.The energy lost through impact is made up for by the robot's walking on a slight decline. This robot builds on the work of McGeer, who built a passive walker with knees, designed with an inner and an outer pair of legs, to prevent motion in the frontal plane and constrain passive walking to an essentially 2D dynamic process, in the sagittal plane [2]. The Collins walker [1] shown above builds on that work, but uses curved feet that enable rocking, side-to-side motions to occur in sync with the forward motion of walking, and uses the arm momentum for yaw stabilization.

Figure 1.4:   Humans are capable of walking on terrain with extremely limited footholds, and even with dynamically coupled footholds such as a slack line. This serves as an inspiration for the places we would like our robots and exoskeletons to operate. Humans are evidence that legged locomotion can be taken to extreme situations with low probabilities of failure (to the degree tolerable by dare devils).

1.2   Review of Exoskeleton Design

Figure 1.5:   HULC (Human Universal Load Carrier) was developed with load carriage in mind, but the device is metabolically detrimental during running.

Exoskeletons have been shown to be effective in a subset of tasks. For those with impaired mobility, exoskeletons such as ReWalk or Ekso Bionics E-legs have been effective in particular assistive scenarios for some people with stroke or spinal cord injuries. These exoskeletons are limited in speed, average walking speeds for paraplegics average at 0.2 m/s [6]

Exoskeletons for unimpaired individuals have been a major thrust of robotics research for nearly two decades as they present the potential to assist an operator during a variety everyday tasks. However, despite this potential, conventional exoskeleton designs such

Figure 1.6:   The Rewalk system shown above weighs 23.3kg and can cost in the range of \$69k to \$85k. The cost is a significant burden to users as of yet health insurance does not cover the use of this device.

as HULC [7] and XOS2 [8] have proven unable to assist with highly dynamic human behaviors like running and in many cases walking. As a result, these devices turn into expensive, heavy exercise machines as they the increase the metabolic burden associated with movement, which has emerged as a primary metric for performance augmentation applications [9].

Recent work, such as the work under DARPAs Warrior Web program, has made significant strides in this area by advancing a new class of lightweight hardware [10], but even these devices have failed to fully capitalize on the promise of exoskeletons. Despite signicant research efforts, there is only one powered mobile device which was developed at MIT [11] which has demonstrated metabolic assistance in a non-stationary task, and
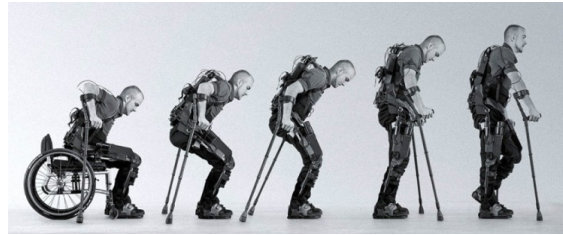
Figure 1.7:   The exoskeletons have shown the ability to restore mobility to those confined to wheelchairs. The Ekso Bionic E-legs shown above have a mass of 20 kg and have a top speed of 0.9 m/s. As can be seen by the added mass studies in Section 4.2, this mass is a substantial and non-negligible load on the user and/or exoskeleton.

it was for walking. While this is a significant result, arguably the most valuable output from this work is the augmentation factor equation which predicts the metabolic benefit of an exoskeleton before testing. While this equation is not without its further questions, it does provide a vocabulary for comparing the burden of mass and the benefit of added power. In this work, we build off the structure of the augmentation factor equation to evaluate how its major components scale as locomotion speed increases, and as the location of added mass along the legs varies.

Chapter 2

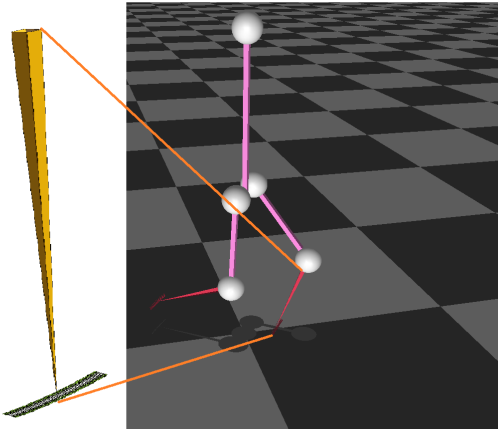# 3D Stabilization

2.1   Introduction

Figure 2.1: The visualization from MuJoCo Simulator is on the right. We placed a magnified view of the curved foot geometry on the left. The center of curvature is 80cm above the foot, arc length of 10 degrees, and fore-aft length is 1.8cm. Since the fore-length of the foot was only 2% of leg length it behaved essentially like a point foot walker in the sagittal plane.

Control of dynamic robots constrained to the sagittal plane has been a focus in our lab [12, 13]. Our sagittal walkers do not exhibit a stable limit cycle in full 3D dynamic simulations, however. Instead, a yaw-roll instability emerges for these point-foot walkers.

Experiments based on anthropomorphic data provide evidence that humans require active control to stabilize an unstable mode in the lateral direction [14]. This motivates the need to stabilize humanoid robots in the lateral plane. Biomechanic studies have identified that humans regulate this with ankle torque [15], lateral foothold placement [14], and abduction of the hip laterally [16, 17, 18]. Several dynamic robots have utilized foot shape to stabilize the lateral direction either with yaw-roll coupling[19] or curvature [1]. Yaw-roll coupling uses a phenomenon similar to that seen in skateboards or bicycles, in which small roll deflections induce a yaw, which then corrects the roll [20]. The concept of curved foot walking toys has been around for over a 100 years [21]. The curvature strategy [22, 1] induces a kinematic center of rotation above the center of mass. The center of mass will oscillate as a stable pendulum with energy dissipation provided by rolling friction and impact events.

While there appears to be a potential trade off between stability and cost of transport [23], a robot designer should also create systems with agility or versatility [24] to navigate the complex terrains of the real world. We make a preliminary exploration of a variety of forward speeds, stride lengths, and stride times. While full 3D dynamics of a robot with multiple degrees of freedom makes analysis difficult, we were able to find trends predicted by step timing. In this paper, we quantify how accurately the 2D dynamics capture the energy efficiency and dynamics of the walker. We center our analysis on the relationship between roll, speed sagittal stepping frequency, and energy consumption.

2.2   Simulator and Models

For the simulations in this paper, we use the MuJoCo Physics Engine developed by Emo Todorov et al. [25]. We use the model parameters of RABBIT for the sagittal plane

[26]. The rotational inertias of each link were considered the same in every direction. Note that typically one would expect yaw inertias of narrow legs to have a lower moment of inertia about the vertical direction (when standing vertically). Because the feet used for simulation had very little yaw dampening, we had to add yaw rotational inertia to reduce yaw oscillations. Typically, 3D walker feet do not use point feet, but instead lengthen the foot's fore-aft length to provide resistive ground yaw moment. A more detailed view of the model can be seen in Fig. 2.1. The lateral separation of the hips, d_{hips} was 0.2m as shown in Fig. 2.4. The robot was completely unconstrained in 3D space and did not have any additional actuators than we used in the 2D models.
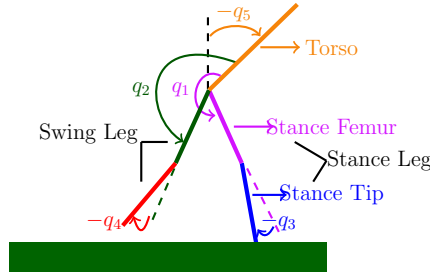
2.3   2D Sagittal Plane System

Figure 2.2: Diagram of the robot from the sagittal plane

We first consider the dynamics constrained to the sagittal plane (shown in Fig. 2.2). Because of this constraint there are no frontal plane coupling effects. The continuous dynamics follow the equation

$$D(q)\ddot{q} + C(q, \dot{q})\dot{q} + G(q) = Bu. \tag{2.1}$$

The 5 links of the walker have 5 joint angles, q; 5 joint velocities, $\dot{q} \in \mathbb{R}^5$; and five joint accelerations $\ddot{q} \in \mathbb{R}^5$. Our robot does not apply any ankle torque making the system

underactuated with control input $u \in \mathbb{R}^4$. We utilize a partial feedback linearization control law stated below

$$u = (H_0 D^{-1} B)^{-1}(v + H_0 D^{-1}(C\dot{q} + G)), \tag{2.2}$$

$$H_0 = \begin{bmatrix} 0 & 1 & 0 & 0 & 1 \\ 0 & 0 & 1 & 0 & 0 \\ 0 & 0 & 0 & 1 & 0 \\ 0 & 0 & 0 & 0 & 1 \end{bmatrix} \tag{2.3}$$

The feedback linearization allows us to directly set the accelerations of the controlled angles with the variable v. We chose the accelerations by using the sliding surface $\sigma \in \mathbb{R}^4$; convergence exponent α; and convergence coefficient k.

$$v_n = -k_n |\sigma_n|^{2\alpha_n - 1} sign(\sigma_n), \quad n = \{1, 2, 3, 4\}, \tag{2.4}$$

$$k = \begin{bmatrix} 40.3791 \\ 96.4343 \\ 77.1343 \\ 15.7245 \end{bmatrix} \quad \alpha = \begin{bmatrix} .7003 \\ .6954 \\ .6991 \\ .7001 \end{bmatrix} \quad \tau = \begin{bmatrix} .0920 \\ .0905 \\ .0632 \\ .1918 \end{bmatrix}$$

The sliding surface σ is determined by the state error h and with time constants τ.

$$\sigma_n = \dot{h}_n(t) + h_n(t)/\tau_n, \quad n = \{1, 2, 3, 4\}, \tag{2.5}$$

The state error h is a function of the current states $q(t)$ and a piecewise reference h_d.

15

$$h(t) = h_0(t) - h_d \tag{2.6}$$

$$h_0(t) = \begin{bmatrix} q_5(t) + q_2(t) \\ q_3(t) \\ q_4(t) \\ q_5(t) \end{bmatrix} \tag{2.7}$$

During the first half of the swing phase, the robot angles satisfy the condition: $q_1(t) + q_5(t) > 180°$. While that condition holds, the reference is:

$$h_d = \begin{bmatrix} 225° & -.968° & -60.0° & TA \end{bmatrix}. \tag{2.8}$$

Otherwise the reference is as follows:

$$h_d = \begin{bmatrix} (269° - \alpha_a) & -.968° & -24.0° & TA \end{bmatrix}. \tag{2.9}$$

We set the fixed reference parameters k, α, τ, and fixed components for h_d from a sagittal robustness optimization (Refer to [27] for more details). α_a is the desired angle of attack of the swing leg before touchdown. Note that the quantity $269° - \alpha_a$ corresponds to the absolute angle of the swing femur. The value TA is the reference that sets the torso angle while walking. During this study we vary TA and α_a in the parameters ξ^s:

$$\xi^s = \begin{bmatrix} \alpha_a \\ TA \end{bmatrix}. \tag{2.10}$$

The feedback control law can be generalized as:

$$u = \Gamma(x, t, \xi^s). \tag{2.11}$$

2.4   Coupled Hybrid Systems

2.4.1   Active Hybrid System-Sagittal Plane Dynamics

We first consider the dynamics constrained to the sagittal plane. The 5 links of the walker have 5 joint angles, q and 5 joint velocities, $\dot{q}$. While our simulation includes all the potential foot dynamics, our standard walking gaits predominately have stationary stance feet. The sagittal states have a continuous time before impact at time t_i, where the subset i represents the step number. This is summarized below as:

$$i = 0, 1, 2, ... \in N \tag{2.12}$$

$$X^s(t_i) = [q \ \dot{q}]^T \in \mathbb{R}^{10}. \tag{2.13}$$

We can numerically calculate the Poincare map, Π^s, to the next preimpact time t_i with a particular deterministic controller u_s:

$$X^s(t_{i+1}) = \Pi^s(X^s(t_i), u_s). \tag{2.14}$$

We have designed a set of sagittal controllers, $U_s \in \mathbb{R}^4$, such that they each have a particular fixed point, X_d^s. The fixed point has this property:

$$X_d^s = \Pi^s(X_d^s, u_s). \tag{2.15}$$

17

This stable fixed point, X_d^s, corresponds to a particular trajectory, which we refer to as the "gait cycle" of the robot. While the above example assumes steady state we assume the robot can have– a steady or unsteady– stepping trajectory called a "gait". We will focus on two gait characteristics: stride length λ, defined as the distance between the stance and swing foot at impact; and stride time T_s, defined as the time elapsing between impacts. We simulate the dynamics forward to develop a sagittal gait map, G^s, which takes an initial condition X_0^s, and controller u_s, to determine the next step's gait parameters:

$$(\lambda, T_s) = G^s(X_0^s, u_s). \tag{2.16}$$

2.4.2   Passive Hybrid System-Frontal Plane Dynamics

The roll dynamics are passive and contain no active control input. We assume no slip contact is maintained by the curved foot. The frontal states are then represented by $X^f \in \mathbb{R}^2$.

$$X^f = \left[\theta_{roll} \; \dot{\theta}_{roll} \right] \tag{2.17}$$

where θ_{roll} is the body roll angle, and $\dot{\theta}_{roll}$ is the body roll speed.

The dynamics take the form of flow and impact separated:

$$X^f(t_{i+1}^-) = \Phi^f(X^f(t_i)) \tag{2.18}$$

$$X^f(t_{i+1}) = \Delta^f(X^f(t_{i+1}^-) \tag{2.19}$$

If the flow and impact are considered together we may take Poincare slices at the instant

before impact:

$$X^f(t_{i+1}) = \Pi^f(X^f(t_i)).$$ (2.20)

Note, there exists a map of the frontal plane dynamics G^f that gives the time until next impact, T^f:

$$T^f = G^f(X^f)$$ (2.21)

As can be seen in Fig. 2.6 G^f has an inverse map, G^{-f} defined at T_s. This would correspond to the instance when $T^f = T_s$:

$$X_*^f = G^{-f}(T^s).$$ (2.22)

For the sake of our constrained 2D frontal plane analysis we will assume that X_*^f could be a stable fixed point in the full 3D system.

2.4.3   Full 3D Dynamics

With full 3D dynamics, the frontal plane dynamics will affect the sagittal plane and visa versa. We will assume for the sake of simplified analysis that our sagittal dynamics controller will still be stable after the coupling of the frontal plane. We then introduce the coupling term C_{sf} to define the effect that the sagittal plane has on the frontal plane's continuous dynamics:

$$X_d^f = \Delta^f(\Phi^f(X_d^f) + C_{sf}(X_d^f, X_d^s)).$$ (2.23)

A condition for stability:

$$\left\|\frac{\partial \Delta}{\partial X^f} \cdot (\frac{\partial \Phi^f}{\partial X^f} + \frac{\partial C_{sf}}{\partial X^f})\right\|_\infty < 1 \tag{2.24}$$

which from the triangle inequality reduces to a more conservative stability condition:

$$\underbrace{\left\|\frac{\partial \Delta}{\partial X^f}\frac{\partial \Phi^f}{\partial X^f}\right\|_\infty}_{=\left\|\frac{\partial \Pi^f}{\partial X^f}\right\|_\infty} < 1 - \underbrace{\left\|\frac{\partial \Delta}{\partial X^f}\frac{\partial C_{sf}}{\partial X^f}\right\|_\infty}_{Coupling\ Term}. \tag{2.25}$$

We equate the left half of 2.25 to $\left\|\frac{\partial \Pi^f}{\partial X^f}\right\|_\infty$—the Jacobian of the Poincare map—using Eq. 2.20, Eq. 2.18, and Eq. 2.19. The right-hand side is the effect of stability of the coupling term. If we assume that the coupling term is small, then the 2.25 could be satisfied with:

$$\left\|\frac{\partial \Pi^f}{\partial X^f}\right\|_\infty < 1. \tag{2.26}$$

2.4.4   Poincare Map of Sagittal System

If we consider i to be the step index

$$i = 0, 1, 2, ... \in N, \tag{2.27}$$

then we can represent the sagittal states as x_i^s to be the state at t_i. Where t_i is the time instant at impact i. While our simulation includes all the potential foot dynamics, our standard walking gaits predominately have stationary stance feet. So we find it necessary

to record the joint angles for the sagittal states.

$$x_i^s = \begin{bmatrix} q(t_i) \\ \dot{q}(t_i) \end{bmatrix} \tag{2.28}$$

We can numerically calculate the Poincare map, Π^s, to the next preimpact time t_i with a particular deterministic controller parameters, ξ_s:

$$x_{i+1}^s = \Pi^s(x_i^s, \xi_s). \tag{2.29}$$

We have designed a set of sagittal controllers, Ξ^s, each with a particular TA and α_a reference parameter. If we pick a controller ξ^s in the set Ξ^s, it has a fixed point, x_d^s. The fixed point has the property:

$$x_d^s = \Pi^s(x_d^s, \xi^s). \tag{2.30}$$

Because our sagittal controllers have large basins of attraction, we simply start the walker at a reasonable initial condition and to see if it converges within 100 seconds of simulation. We exclude any gaits that do not converge or that fall down from our analysis.

The two gait characteristics that we focus on are stride length λ, defined as the distance between the stance and swing foot at impact, and stride time T_s, defined as the time elapsing between impacts. We define G^s as the map (superscript "s" denoting the sagittal constrained system) that extracts these parameters given an initial condition and controller. We use the fixed point, x_d^s, as the initial condition and a particular controller u_s to determine the limit cycle's gait parameters:

$$(\lambda, T_s) = G^s(x_d^s, \xi^s). \tag{2.31}$$

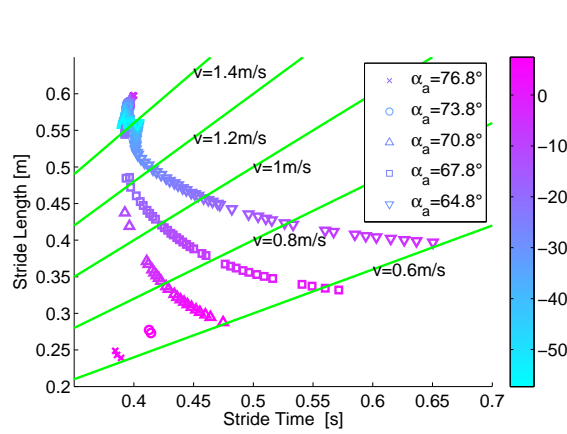## 2.4.5   Varying Set of Sagittal Controllers

Figure 2.3: This figure depicts the gait space spanned by G^s through the variation of two control reference parameters, α_a and TA. The gait characteristic is at the steady fixed point of the controller on flat ground. The green lines are provided as reference for isocurves of constant forward velocity.

We first adjusted the angle of the torso by varying the reference angle, TA. In general, forward leaning has been linked to faster forward speeds [28]. As can be seen in Fig. 2.3, forward torso leaning (negative angles) successfully produces faster walking in our models. This appears to be due to a combination of shorter step times and longer stride lengths. To more fully span the gait space, we also varied the swing femur angle, $q_1(t)$, at touch-down through the variable α_a. α_a has a more direct effect on the step length, because it controls how far the robot extends the swing leg. We tested angles of attack α_a from 64.8° to 76.8° in 3° intervals. The torso angle, TA, was from $-57°$ to 7° in .5° intervals. We examined only each controller's steady state gait characteristics. Examining transients from various initial conditions and controller switching is a topic for future work. (Refer to Fig. 2.3 for the full details of gaits generated.)
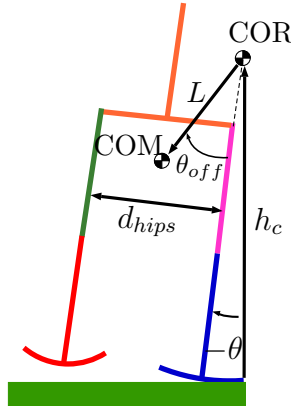
Figure 2.4:   Each foot has a center of rotation (COR) placed directly above its respective hip. The height (h_c) above the ground of the COR is 0.8m. The system behaves very similarly to a stable pendulum with length L, except that there is a pendulum offset, θ_{off}.

2.5   2D Frontal Sway Analysis

2.5.1   Curved Foot Design

We use the design method from [22] of matching pendulum resonance with the step frequency. Nominally, we started our design with a baseline step period of $T_s = .35s$. The curvature of the foot defines center of rotation (COR). The distance between COR and COM is called the pendulum length, L (refer to Fig. 2.4). We model the frontal plane simulation with all sagittal joints held statically at $q(t) = 0$. This stable pendulum has a a half period of

$$T_{pendulum} = (\pi)\sqrt{\frac{L}{g}} \approx .35[s] \ . \tag{2.32}$$

For our design, we chose $L = 12.21$ centimeters to match our baseline gait. We do not change this parameter for any of the experiments. Our goal is to see the versatility of this fixed curvature design for different types of gaits.

2.5.2 Isolated Frontal Plane Dynamics

Note that the $T_{pendulum}$ term is derived using many course approximations and a very rough small-angle linearization of the full dynamics, making it an approximation. We therefore consider it more accurate to consider the nonlinear uncoupled frontal plane dynamics of the roll angle θ. The frontal plane dynamics can be more accurately represented with pendulum length L, total mass $M_t = 32\ kg$, and rotational inertia of the whole robot, $I_{com} = 6.1\ kg\ m^2$:

$$(I_{com} + M_t R_c^2)\ddot{\theta} + L\ M_t\ g\ sin(\theta_{off} - \theta) = 0. \tag{2.33}$$

where θ_{off} is an offset angle defined by the geometry as:

$$\theta_{off} = sin^{-1}\left(\frac{d_{hip}}{2L}\right) \tag{2.34}$$

and the variable R_c is the distance from the foot contact point to the center of mass. Note that $h_c = 0.8$ m is the height of the center of rotation above the ground. This quantity squared can be calculated with the law of cosines by:

$$R_c^2 = L^2 + h_c^2 - 2h_c Lcos(\theta_{off} - \theta). \tag{2.35}$$

2.5.3 Poincare and Gait Map of Isolated Frontal Plane

The roll dynamics are passive and contain no active control input. We assume slipless contact is maintained by the curved foot. The frontal states are then represented by x_i^f
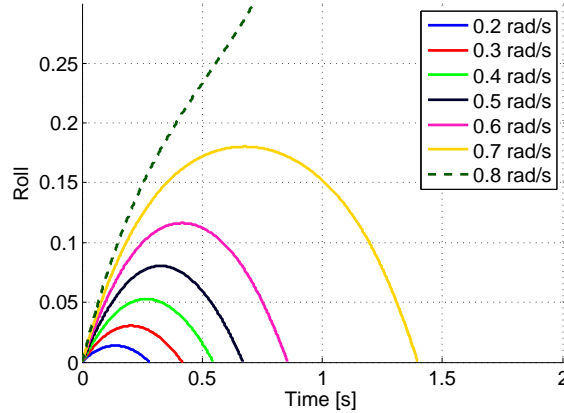
24

Figure 2.5: To determine times of return the model was simulated with various initial roll speeds. The dashed line signifies an initial roll speed in which the robot tips over. Roll is denoted in radians. Since this trajectory never recovers to $\theta = 0$, the time return map is undefined for this velocity.

at impact i with only the body roll speed, $\dot{\theta}$, because impacts happen when roll is 0.

$$x_i^f = \left[\dot{\theta}(t_i) \right] \tag{2.36}$$

When we simulate the frontal plane in isolation there exists a gait map G^f (super script "f" denotes frontal plane constrained) that for a given initial condition x^f will have T^f time till the next impact.

$$T^f = G^f(x^f) \tag{2.37}$$

As can be seen in Fig. 2.6, G^f has an inverse map, G^{-f} defined at T_s. This would correspond to the instance when $T^f = T_s$.

$$x_d^f = G^{-f}(T^s) \tag{2.38}$$

We assume that x_d^f of the 2D frontal system could be a stable fixed point of the full 3D simulation. While the uncoupled system would not hold on this fixed point due to energy losses (impacts and rolling friction), we will assume the coupling from the sagittal plane

pumps in sufficient energy.

The assumption of a linearized pendulum might make one expect a flat timing map ($T_{pendulum} = G^f(x^f)$ for all x^f). The actual timing map for the nonlinear oscillator was numerically determined and is shown for the curved foot design in Fig. 2.6. The timing map prediction was done by simulating the frontal plane system in isolation. A given initial roll speed would correspond to a particular time until next impact. As can be seen in Fig. 2.6, the 2D uncoupled system closely resembles the full 3D performance. The 3D system has the same general trend that faster roll velocities correspond to longer step times.
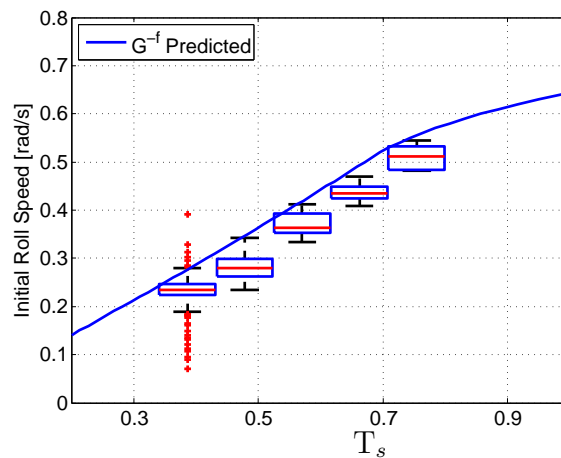

Figure 2.6: G^{-f} timing map above is calculated running isolated frontal simulations such as those shown in Fig. 2.5. The full 3D dynamic simulation is represented with the box and whisker plots. The box is the 25-75% interval, while the bars represent the 9% - 91% interval. Outliers are plotted with red crosses and we suspect they are more prevalent at shorter time steps due to the larger number of gaits. The frontal plane system behaves overall very similarly to the full 3D dynamical system. The longer stride time of the 3D system, is likely due to the fact that impacts do not happen exactly at $\theta = 0$. Instead, impacts are delayed by swing leg retraction. The robot has to roll further, which takes a longer time.

2.5.4   2D Curved Foot Energy Dissipation

Because frontal plane dynamics are dissipative with rolling friction and impact losses, we assume energy must flow from the sagittal plane to the frontal plane to keep it oscillating. We define $E_{frontal}$ as the extra energy necessary to run the 3D model compared to the 2D model over one step.

We try to approximate the energy lost in the frontal plane with the Hamiltonian, $\mathcal{H}$. The Hamiltonian represents the current energy in the system E_i at step i:

$$\mathcal{H}(x_i^f) = Kinetic + Potential = E_i. \tag{2.39}$$

The energy dissipated over one cycle is approximated as:

$$
\begin{aligned}
E_{frontal} &\approx E_{i+1} - E_i \tag{2.40} \\
&= \mathcal{H}(\Pi^f(x_d^f)) - \mathcal{H}(x_d^f) \tag{2.41} \\
&= \mathcal{H}(\Pi^f(G^{-f}(T_s))) - \mathcal{H}(G^{-f}(T_s)). \tag{2.42}
\end{aligned}
$$

Our simplified 2D frontal plane analysis shows a prediction in Fig. 2.7. This prediction trends towards higher energies required at longer step times. This can be explained by greater energy losses from impacts in the frontal plane. As can be see in Fig. 2.6, longer step times correspond to larger roll velocities during impact events.

While we studied a large number of stable gaits found in 2D and 3D walking, $\alpha_a = 67.8$ and $\alpha_a = 64.8$ were the only data sets where 3D and 2D gaits were comparable. As can be seen in Fig.2.9 these were the only two data sets that had a range of 2D stride times similar to the range of 3D stride times. Parts of these data sets had minimal stride time and stride length changes from 2D to 3D. As can be seen in Fig. 2.7 the general trend upheld, as predicted by our analysis. Oddly, for shorter stride times, gaits actually

became more energy efficient than their 2D counterparts. Whether there is beneficial energy storage in the frontal plane, or shifting of the sagittal gait characteristic that can explain this phenomenon, is a subject for future work.
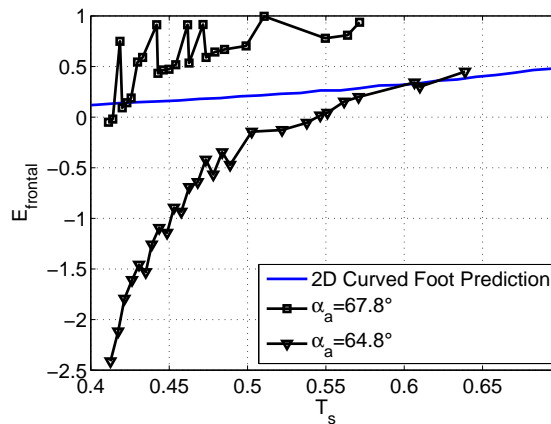

Figure 2.7: The black data points represent the difference in energy of sagittal constrained and full 3D simulations. The 2D curved foot prediction is based on the frontal plan analysis present in Eq. 2.42. The units of energy are joules per step. The data sets $\alpha_a = 67.8$ and $\alpha_a = 64.8$ had minimal changes in the sagittal planes stride length and stride time in 3D. This allowed us to more easily isolate the effect of adding frontal plane dynamics. Note that the sagittal consumption of energy ranged from 10 to 35 J per step.

2.6 Full 3D Dynamics Simulation

2.6.1 3D Shifting of Gait Characteristics

As expected, there was a shift in the gait characteristics of the 3D walking from the 2D model. We suspect that the stride was more susceptible to 3D variations because our controller enforces references based on angles, not on specific timing. In general, the walkers walked with slower forward speed due to the slower step times. The walking speed variability was due to changes in both stride length (Fig. 2.8) and stride time (Fig. 2.9).
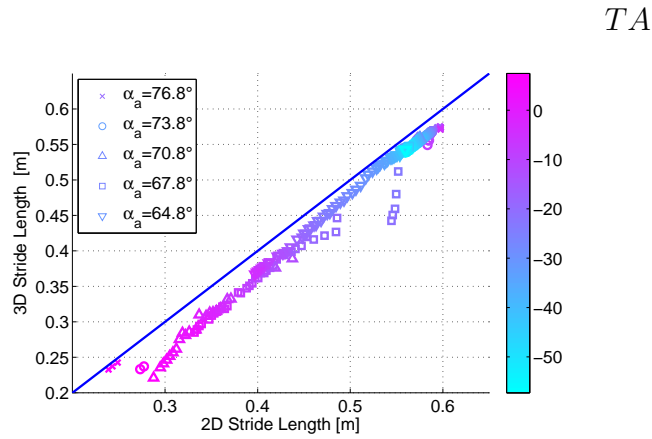
TA

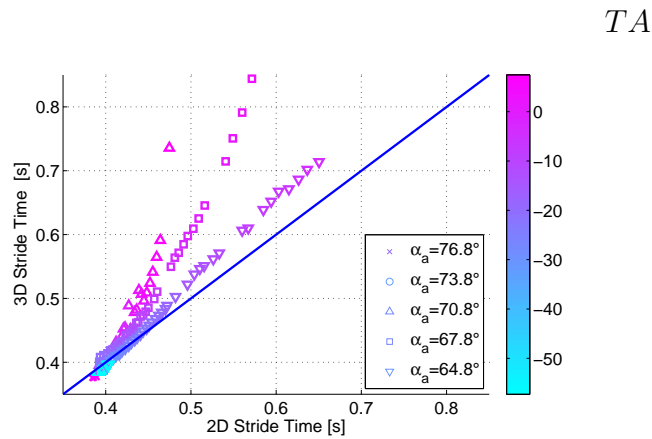Figure 2.8: step length change from 2D to 3D. Color bar represents torso angle.

TA

Figure 2.9: Stride time change from 2D to 3D. Color bar represents torso angle.

2.6.2   Energy Consumption

We define the mechanical power flux, P_n, at each actuator (n index 1 through 4):

$$P_n(t) = \omega_n \cdot \tau_n \quad n = \{1, 2, 3, 4\}. \tag{2.43}$$

We use two different work metrics for the robot. First we consider conservative work, which penalizes both positive work and negative work. Walking gaits had a high amount of variability in performance, as can be seen in Fig. 2.10. We consider this a more

accurate representation of the energy required by real actuators, such as electric motors.

$$COT_{conservative} = \frac{\int_0^{T_s} \sum_n |P_n(t)| dt}{M_t g \lambda} \tag{2.44}$$

Finally, the last metric we evaluated was the net mechanical energy, which assumes that the actuator can recover negative energy. For practical robots, actuator losses make reaching this level of energy efficiency impossible. Human metabolic cost of transport is 5 to 6 times above the mechanical cost of transport. We instead use this metric to look for increases in energy in changing to 3D dynamics.

$$COT_{net} = \frac{\int_0^{T_s} \sum_n P_n(t) dt}{M_t g \lambda} \tag{2.45}$$

Note that as can be seen in Fig. 2.11 there was a general trend for the COT to go up at higher speeds. Generally, increases in walking speeds cause larger expenditures of energy in humans. The small decrease in energy expenditure in 3D gaits can be explained by short stride times—0.35 to 0.4s—of gaits in the 1.3 m/s range. Remember the trend of energy savings at shorter stride times seen in frontal plane dynamics (shown in Fig. 2.7). The controllers used were not optimized for energy efficiency, so a certain amount of variability is expected. We expect 2D energy efficiency variability to also be reflected in the 3D gaits.

2.7   Conclusion

An uncoupled assumption allowed us to develop the sagittal plane and frontal plane stabilization separately. As expected, there was a shifting in the sagittal gait's stride time characteristics. We mainly saw a shifting of the stride time, as the controller is driven by a phase variable rather than time reference tracking.
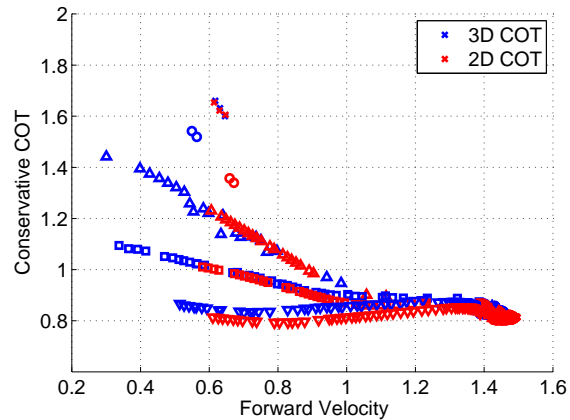
Figure 2.10: This COT corresponds to the work in Eq. 2.44. Interestingly, the conservative COT goes up with slower speeds. Humans also show a increase in metabollic expendature at walking speeds below 1 m/s.[29]. This supports the thought that a larger amount of negative work is required to walk at slow speeds. The effect of the frontal plane dynamics appear to be negligible compared to the cost of negative work.

The coupled frontal plane dynamics (Fig. 2.7) matched closely with our uncoupled prediction. Faster roll speeds were correlated with longer step times. Intuitively, this makes sense – if you push a stable pendulum with more radial speed, it will take longer to return. This dynamic trend correctly predicted higher energy consumption of 3D walkers at longer stride times. While this general upward trend did hold, there was large variation between data points. We expected this because the 3D dynamics can shift the sagittal gait into a more efficient regime – for example, slowing down the walker. As can be seen in Fig. 2.11, slower forward speeds in the sagittal plane correlated with less energy expenditure. When the 3D walker slows down in the sagittal plane due to coupling, it can shift to a more efficient walking gait. Our methods were good for predicting the general dynamical behavior and general energy trends, but the intricacies of 3D walking introduced a great deal of variability to the data we observed.
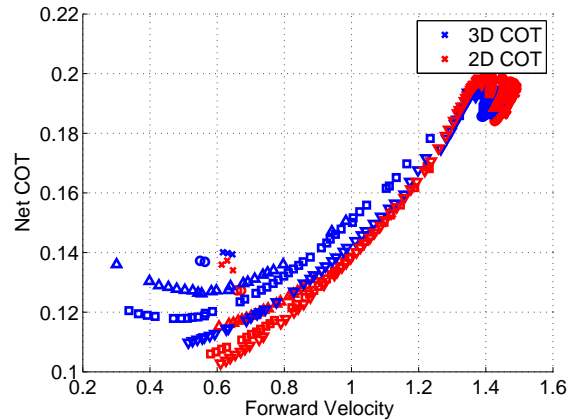
Figure 2.11: Cost of transport corresponding to Eq. 2.45. Note that in general faster walking speeds correlated with more energy expenditure for the 2D gaits. Remembering that adding the frontal plane dynamics for 3D walking results in energy efficient gaits at shorter stride time (as seen in Fig. 2.7), we can explain why the 3D walkers are more efficient at higher speeds (1.2 to 1.5 m/s). The faster walking gaits corresponded to short stride times of .35 to .4 [s] (Fig. 2.3)

2.8   Future Work

While the curved foot walker is usually designed for a particular stride frequency, we show it capable of supporting a variety of 3D dynamical gaits. Additionally, we plan to investigate the energy savings observed in some 3D gaits. We suspect that this may be due to beneficial energy storage of energy in the frontal plane or a shift of the sagittal gait to a more efficient regime. We plan to extend these principles to design an active laterally stabilized walker. Our preliminary active lateral stabilization has shown similar energy efficiencies. Additionally, we have found techniques for reducing the sagittal gait coupling disturbance. The active lateral stabilization results will be released in a subsequent paper.

For this paper, the sagittal gait map G^s was tested with steady state limit cycles; it would be interesting to examine its transient solutions. For example if the walker is run in steady state with a certain step length, how quickly can the robot transition to a new step length? This information could then be used for realtime foothold placement

selection, which would be necessary for environments with intermittent footholds. The computability of this map may be challenging due to the high dimensionality of the system ($\mathbb{R}^{22}$), also known at the "curse of dimensionality." We plan to see if our meshing algorithms can be used to reduce the problem's dimension to a computationally feasible problem [30].

Chapter 3

Agile Foothold Placement

3.1 Motivation for Agility

Figure 3.1: Unimpaired humans can cross a variety of terrains with low probability of falling. Here we examine the stepping stone problem, where feasible footholds are in limited locations. Between feasible footholds are gaps that are unreliable footholds. With sufficient foothold humans can quickly find solutions to this type of problem and with limited planning traverse terrains as shown above.

While dynamic walking has proven to be extremely energy efficient, it is lacking in its ability to traverse limited footholds. We believe switching low level controllers may be a simple way to give dynamic walkers foothold placement selection. We propose utilizing meshing framework to characterize the agility and stability of switching algorithms. The agility of these switching controllers will be quantifiable by the space spanned by our

mesh (reachable space) and its connectivity properties. Additionally, the structure of the mesh will classify the types of intermittent foothold that may be successfully traversed.

3.2   Energy Efficient xor Agile Robots

Legged robotics offer the ability to traverse terrains that are impassable to more traditional wheeled robotics. Existing walking robots do not offer both efficiency and versatility [3]. The more traditional ZMP movement robots dynamically constrain the robot for the purpose of guaranteeing dynamic stability [31]. The conservative criteria for stability [32] restricts the permissible motions and creates motions with low cost of transport. Humans offer inspiration that agility can be achieved without sacrificing energy efficiency. Humans have a low mechanical cost of transport of .05 [4] yet are still capable of traversing much more complex terrain than robots.

Research has been done to explain how humans achieve extremely efficient locomotion and how to reproduce it in robots. Passive dynamic robots in the 1980s showed that exploiting the system's natural dynamics could yield stable walking cycles [2]. Active robots have been able to incorporate some of the energy saving mechanism of passive dynamic robots. A recent example is the Cornell University ranger robot, which demonstrated a cost of transport of .28 in 2010 [5]. While it had impressive energy efficiency, this robot lacked foothold placement selection and only limited turning abilities. Hybrid zero dynamics (HZD) presents a good framework for solving periodic gaits with energy efficiency on flat terrain [33]. This framework has been extend to include occasional one-step aperiodic transitional gaits [34]. Using high level policies, such as a finite state machine [35], one can more robustly walk on uneven ground heights. Additionally, Saglam and Byl have developed robust switching policies for HZD walking on uneven terrain [36].

The agility of humans and robots is lacking good metrics to describe the gap we can qualitatively observe with the passable terrains. As robots at the DARPA Robotics Challenge demonstrated, robots are getting better at sensing and planning locomotion in complex terrain. But the optimization techniques employed require significant computing power and detailed terrain information; the robot can take several minutes to traverse a pathway that would take only seconds for the average human. Humans are capable of operating quickly and with incomplete information. Mattis and Fajen experimentally showed that humans retain accurate foothold placement with only a two-step visibility horizon [37]. With limited information and time to decide foothold placement, it is unlikely that humans are doing complex optimization or traversing large decision trees. A possible explanation is that humans have a small set of control strategies that allow for robust, stable, and agile motions. In this chapter, we examine how a small set of controllers can can yield energy efficient gaits in environments with randomly placed intermittent footholds.

3.3   Quantifying Stability in Agile Robots

Note that unsteady gaits are ill suited for traditional stability tools. Linear analysis generally looks for a fixed point in the state space which, solutions contract towards. This analysis can make sense for quiet standing but is not possible for dynamic walking. Traversing a complex non-linear space makes it difficult to give convergence guarantees.

Another solution is to utilize limit cycle stability. As can be seen in Fig 3.2 trajectories converge to the same path in phase space. They do not necessarily converge to each other in time. A common approach for dynamic walking is to find stable limit cycles. Stability of this limit cycle can be Poincare map analysis. For example, if the state of the robot is represented by X^i at the ith impact for a deterministic system there exists a Poincare
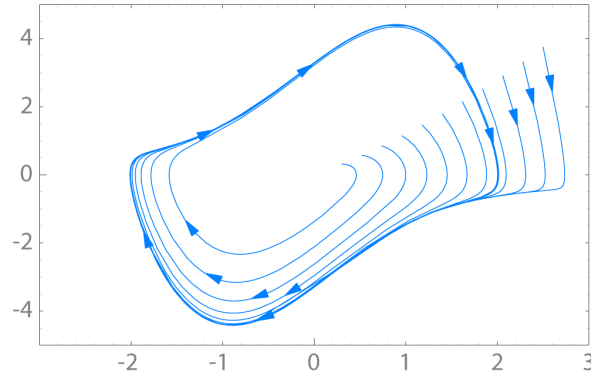
Figure 3.2: Here the Van der Pol occilator exhibits a stable limit cycle. Trajectories do not converge to each other in time, but instead converge to a common path.

map, Π. The map is dependent on the state of the robot, X^i, and the control used for the next step, u.

$$X^{i+1} = \Pi(X^i, u) \tag{3.1}$$

If the controller, u^f, has a stable limit cycle, then there will be a state X^f at impact with the ground.

$$X^f = \Pi(X^f, u) \tag{3.2}$$

Generally, one will numerically approximate the Jacobian, $\frac{\partial \Pi(X^i, u^f)}{\partial X^i}$ around the fixed point. It is sufficient for local stability if all the Jacobian singular values are less than or equal to 1.

$$\left\| \frac{\partial \Pi(X^i, u^f)}{\partial X^i} \Big|_{X^i = X^f} \right\|_\infty \leq 1 \tag{3.3}$$

A non-linear approach to stability seeks to define a basin of attraction (BOA). If one can analytically prove stability using linear analysis for a set of points, one can extend this stability to a larger region by proving convergence to the stable set of points. The basin of attraction is a set of initial conditions that will converge towards a stable set. As an example, Gregg et al. [38] applied this technique with a set of stable controllers

for a bipedal robot [38]. They first presented evidence of the stability of each controller in isolation and then extended it to the group. The stability of switching controllers was guaranteed by insuring that switches only occurred in the BOA of the next controller. While breaking apart a complex problem into smaller stability problems makes formal mathematical analysis more tractable, it possibly oversimplifies the problem and excludes important legged locomotion.

Nature has shown plenty of examples of animals using agile dynamic locomotion that can adapt to their enviroment. For examples, mountain goats are able to nimbly move on intermittent footholds for grazing that is inaccessible to less nimble animals. As evolutionary pressures allow for a small number of failures (as long as enough individual survive to reproduce), the strategies employed by these animals may not pass strict mathematical proofs of stability. Because a strategy that works the majority of the time but has small probabilities of failure is still useful, we need mathematical tools and metrics to understand this space.

Traditional stability tools are designed to give a binary outcome of "stable" or "not stable" when all information for dynamics and controls is provided. As animals are likely operating with an incomplete or inaccurate model of the world (they can see only so far ahead), they likely don't have such a stringent view of stability. A reasonable hypothesis is that metastability [13] is one way to deal with uncertainty about the environment. We look to use our meshing technique to offer confidence about stability by forward simulating the model in a variety of scenarios. We make it computationally efficient by discretely building out the state space and reusing simulation solutions to avoid extra simulations.

3.4   Approach

We plan to explore the space of controller switching without periodic or stability constraints. We propose meshing as a means to discover the span of the stable reachable space. We are capable of exploring the reachable space for a small set of controllers on rough terrain [36] for 5-link walkers. If we can select a small subset of controllers that span the foothold placement space, we believe switching between them will allow traversal of limited foothold terrain. We plan to use dynamic programming to solve for a high-level switching policies that traverse terrain with intermittent footholds.

3.4.1   Generation of Low Level Controllers

The trajectory, $x(t)$, fully describes the joint angles and velocities of the robot. During the swing phase of walking it can be fully described as:

$$\dot{x}(t) = f(x(t)) + g(x(t))u(t). \tag{3.4}$$

During normal walking, the continuous dynamics should periodically impact the ground at time t_i where i is the step index. Impacts occurs when the state $x(t_i) \in S$, where S is set of states for swing foot impacting. The preimpact state $x^-(t_i)$ gets mapped to the post impact state $x^+(t_i)$ by the impact dynamics:

$$x^+(t_i) = \Delta(x^-(t_i)) \tag{3.5}$$

For brevity we will write $x_i := x^-(t_i)$ to mean the preimact state at step i. Note that x_i contains a step length λ_i as the separation between the feet in double support. So by keeping track of the preimpact state we are also mapping out the possible step lengths.

To vary the step lengths from step to step, we will use parameterized control laws.

Each control law is simply a function of the current state x and the controller parameters ξ.

$$u(t) = \Gamma(x(t), \xi(t)) \tag{3.6}$$

We make this a switching controller by adjusting $\xi(t)$ at every time step. It can be written as a piecewise function as follows:

$$\xi(t) = \begin{cases} \xi_0 & t_0 \leq t < t_1 \\ \xi_1 & t_1 \leq t < t_2 \\ \quad \vdots \\ \xi_i & t_i \leq t < t_{i+1} \end{cases} \tag{3.7}$$

For shorthand we will write $\xi_i := \xi(t_i)$ as the control parameters for step i. We will restrict the controller parameters to a finite set, $\xi_i \in \Xi$. Ξ is the finite set of allowable control parameters. We have experience setting step length and step time with two reference parameters in full 3D walking [39]. The Poincare map, Π, maps one preimpact state x_i to the next x_{i+1} as a function of the ξ_i control parameter.

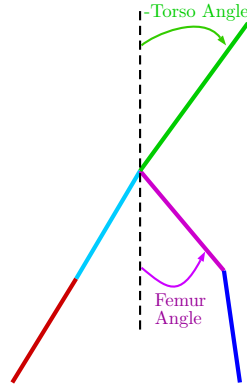$$x_{i+1} = \Pi(x_i, \xi_i) \tag{3.8}$$

Figure 3.3: Utilizing the torso angle reference, TA, and femur angle of the swing leg at touchdown, FA, it is possible to regulate both the step time and step length of the robot. Refer to Fig.3.4 for the space spanned.
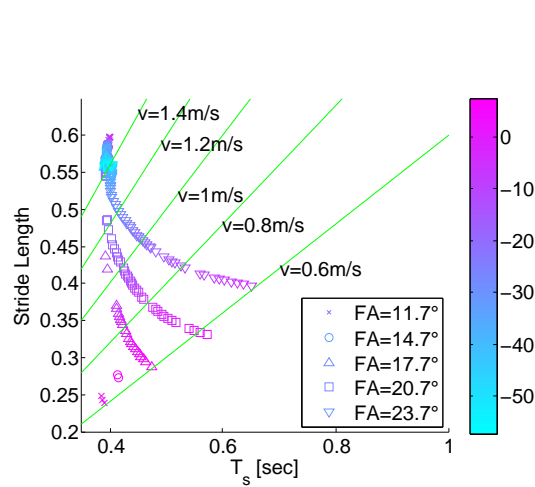
TA

Figure 3.4: Solely by varying the control reference parameters FA and TA described in Fig. 3.4.1, we were able to find a wide variety of gaits. We specifically looked at the step time, Ts,(commonly referred to as the time till next impact) , and the stride length, which was the distance traveled in one step. Note that these gaits were from the controller's stable limit cycle on flat terrain. The green lines are provided as reference for isocurves of constant forward velocity.

41

3.4.2   Meshing of Reachable Space

For a small set of Ξ we plan to calculate the reachable set $R(\Xi) \subset X$ through forward simulations. We will represent it with a mesh, M, more rigorously defined as:

$$M := R(\Xi) \cap S. \tag{3.9}$$

The mesh M will be discretely approximated with a finite number of regions X^r.

$$M \approx \{X^{r1}, X^{r2}...\} \tag{3.10}$$

X^{ri} is a region in S near a certain point x^{ri} by a distance δ:

$$X^{ri} := \{x| \ \|x - x^{ri}\| < \delta, x \in S\} \tag{3.11}$$

Note that the mesh and the Poincare map can be represented as a directed graph– a toy example is shown in Fig.3.5. Each node of the graph is a discretized region in the mesh, and the directed arrows represent the Poincare map. A particular control policy is simply a path through this directed graph. Note that we consider all the points in the region X^{ri} to have average step length λ^{ri}, which is shown on the graph. Given a terrain with intermittent foot holds, the ability to find a feasible policy, or path, is directly related to the connectivity and variety of step lengths attained along that path.
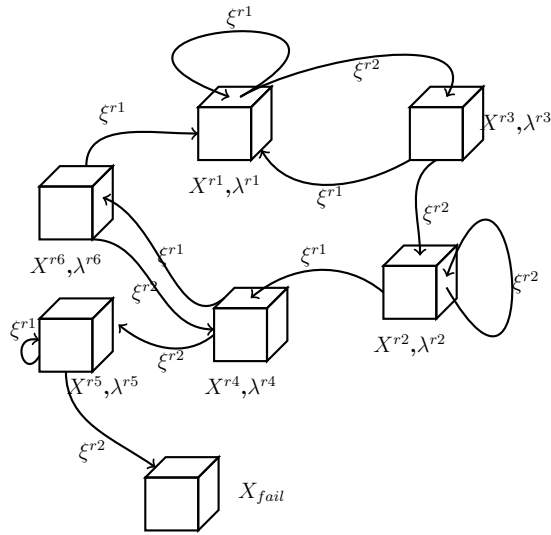
Figure 3.5: This is a toy example with $\Xi = \{\xi^{r1}, \xi^{r2}\}$ as the parameter space. Each cube represents a region X^{ri} in the mesh, that region has an associated step length λ^{ri}. Each arrow represents the Poincare map Π. For example, the top-most edge in the example represents $X^{r1} = \Pi(X^{r1}, \xi^{r1})$. Note the region X_{fail} represents any configuration in which the robot falls down. No arrows transition away from this state because we consider recovering from a failed position beyond the scope of this study.

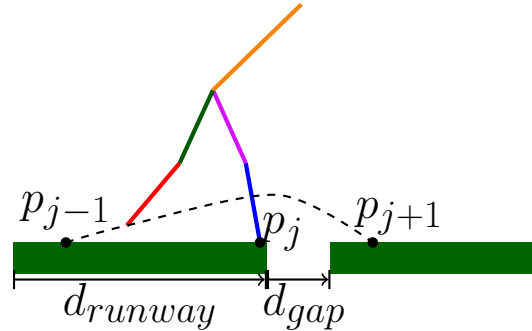### 3.4.3   Foothold Avoidance Problem

Figure 3.6: The robot is challenged with placing a certain number of steps on only feasible locations. The stance foot positions labeled as p_i must lie in the feasible space.

One of the main advantages of legged locomotion over wheeled locomotion is the ability to traverse terrain with intermittent footholds. Here we examine the sagittal plane case of intermittent footholds.

Problem Definition: Find series of $j+1$ steps that places the robot on the passible terrain after the gap given:

1. initial conditions of the robot X_0,

2. initial foot placement p_0,

3. a space of passable terrain d_{runway} between the current foothold and the start of an obstacle,

4. a gap of width d_{gap} which no footholds can be placed,

5. passable terrain after the gap.

We plan to test the connective properties of the mesh in solving foothold placement problems, such as shown in Fig. 3.6. We will utilize dynamic programming to solve for feasible policies over a finite step horizon. We believe we can equate this problem to

a knapsack problem, fitting a finite amount of step lengths in a fixed length of feasible footholds before a gap. Our goal is to utilize our knowledge of the connective properties of themes to give a continued guarantee of stability. In this case, we mean stability in the sense of not falling down. We do not need to use limit cycle stability. Instead, we use the connectivity of the mesh to form stability conditions such that the robot can remain in the stable portion of the mesh (states that don't lead to failure in finite time).
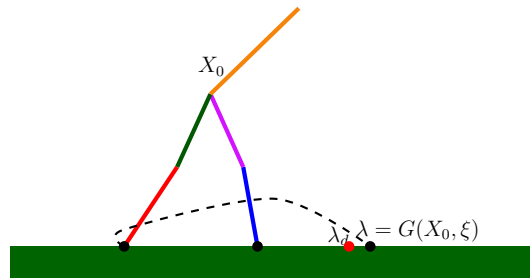
3.4.4   Foothold Selection Problem

Figure 3.7: The red dot represents the desired foothold λ_d. With a given initial condition, X_0, the robot is capable of applying the control parameters, ξ, to achieve a step length of λ.

Foothold avoidance is dependent on the ability of the robot to be able to choose its steps. If presented with areas on which it cannot step, it must examine the footholds that it can take. To test how well the robot can choose a foothold, we present the foothold selection problem. The foothold selection problem is given a desired foothold and robot's intial configuration, X_0, how close can the robot place its foot to the desired foothold? That is to say:

$$\underset{\xi}{\mathrm{argmin}}(G(X_0, \xi) - \lambda_d)^2 \tag{3.12}$$

The gait maps, G, is a reduced form of the one presented in Eq. 2.16. The gait map

takes a controller ξ and initial condition X_0, which map to a step length λ.

$$\lambda = G(X_0, \xi) \tag{3.13}$$

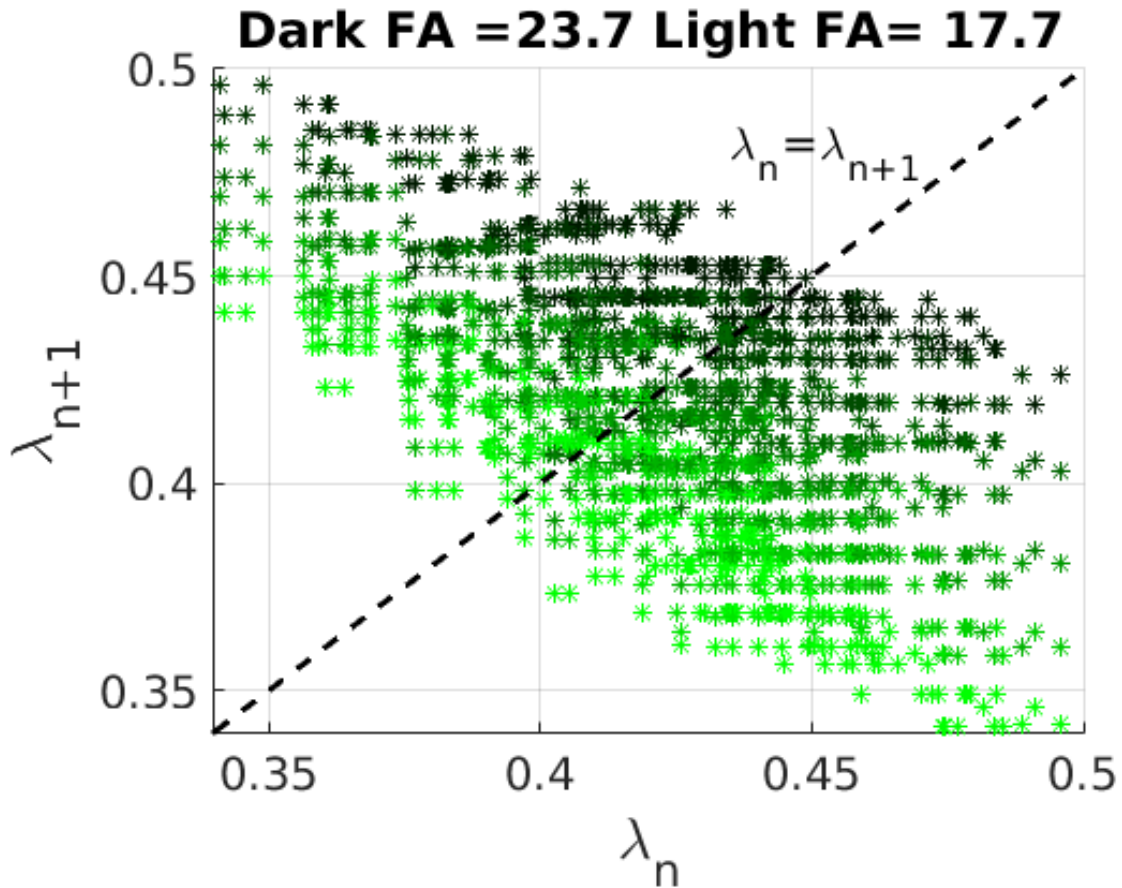## 3.5   Results

3.5.1   Agility Mesh

Figure 3.8: This figure depicts the next step length, λ_{n+1} depending on the current step length, λ_n. (Refer toEq.2.10 for reference of the FA use in the controller.) The FA represents the swing leg's femur angle at touchdown. Lighter green colors represent more vertical femurs at touchdown, which correlates with shorter step widths.

The mesh vastly expanded the possible footholds, and the number of options for the subsequent footholds as can be seen in Fig. 3.8. Note, also, that fixed point analysis would only have found a subset of the points. Note all fixed points are constrained to lie on the $\lambda n = \lambda_{n+1}$. The agility mesh instead has the ability to utilize transient solutions which are normally ignored in fixed point analysis. Note that Fig. 3.8 gives us a sense of
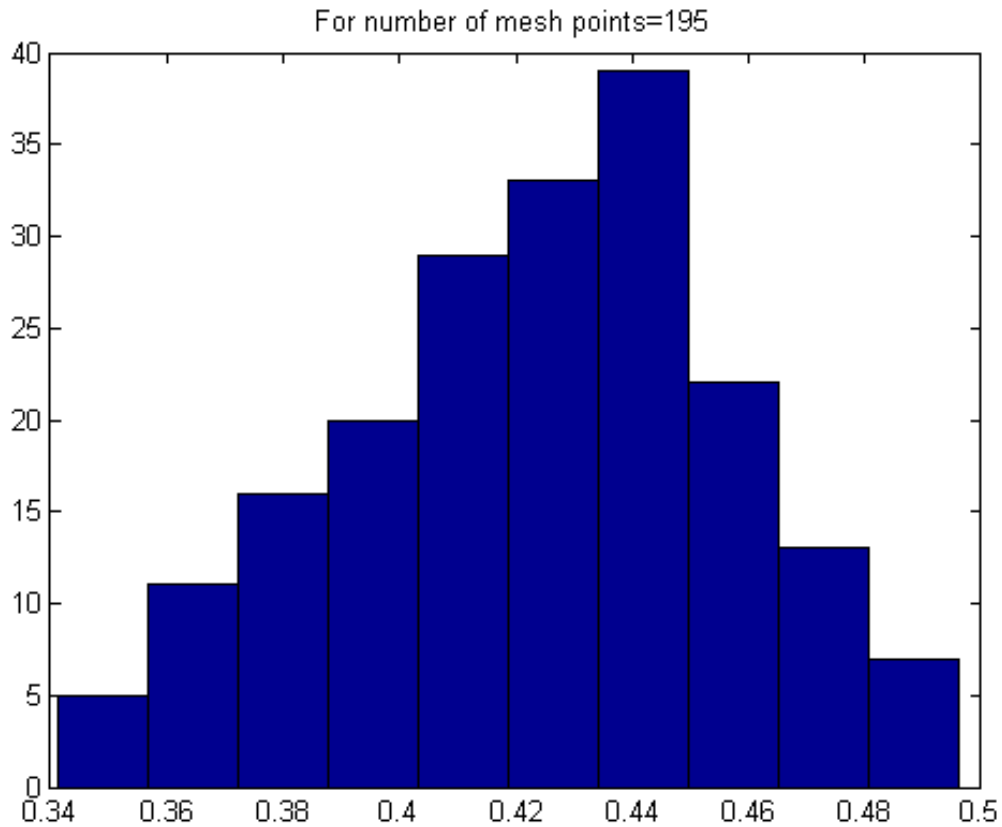
For number of mesh points=195

Figure 3.9: The mesh shown in this example utilized 195 points. This was distributed over a range from 0.34 to 0.49 m. Note that this is a range of 42 to 61% of leg length.

how well connected the space is. For example, if the robot had the need to take a specific series of steps such as 0.4m and then a 0.45m step, there are solutions in the reachable space.

Note that if we had more controllers to the mesh, we could potentially fill out the missing agility space. The controllers do not have to be stable in isolation, as their one-step effects may be modified and stabilized via future control actions. Instead, one can include unstable controllers to introduce wide variations in step width. Humans are capable of exhibiting transient extreme motions- for example doing feats such as long jumping. There can be intermediate steps that are impossible to repeat, but the final

step (the jump), can only with preperation. This concept has been illustrated in related

work by our lab [40].

3.5.2   Connectivity of Mesh

Each region X^r is a node, and each directed edge is a decision to use ξ_i. The edges will be associated with the next step's control parameters. Each node represents a set of points that are in close proximity and behave similarly. We can find a strongly connected set of nodes in the graph, meaning it is possible to reach any node from any other node in the set. The strongly connected set represents the stable reachable set which controller policies can switch between. In the toy example given in Fig.3.5 the state $\{X_1, X_2, X_3, X_4, X_6\}$ forms a strongly connected set. Note that X_5 is excluded because it is not possible to return from it to the rest of the nodes. A switching policy ensures the robot in the strongly connected set will be agile and stable. Agility can potentially be inversely related to the maximum shortest path between any two nodes. That is to say an agile walker has the ability to choose a variety of next steps. A switching policy may not be limit-cycle stable, but it could be broadly stable in the sense that it does not visit the failure state.

The low level controller in Eq. 3.6 will have a piecewise constant reference during the duration of a step. We will explore switching reference at the beginning of each new step. This will allow us to compute the reachable space, as well as the controllable space. We present a toy example in Fig.3.5 where there are only two control parameters ξ_1 and ξ_2 from which to select. We start the search our initial stable fixed point set $\mathbb{X}_f = \{X_1, X_2\}$. X_1 is the fixed point corresponding to ξ_1 and X_2 corresponds to ξ_2. From the breadth first search we can find the reachable set

$$R(\mathbb{X}_f) = \{X_3, X_4, X_5, X_6\}. \tag{3.14}$$

We then define the controllable set as: $C(X_i, X_j)$
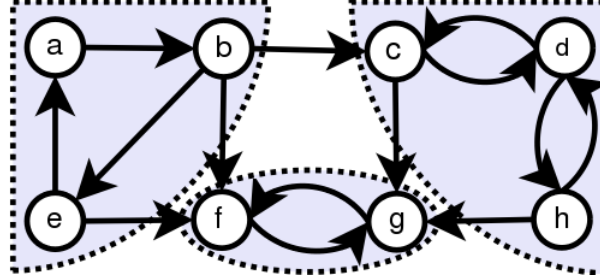
3.5.3 Using Mesh for Stability Proofs

Figure 3.10: This figure [41] gives an example of three strongly connected sets. For example, "a", "b", and "e" are a strongly connected set. A policy that considers only edges that stay in the connected set does not have to worry about its reachable space contracting. For example, if the transition from "b" to "f" was considered, then the robot would no longer have the ability to reach b.

The mesh can be used to give some guarantees of stability for a switching controller policy. This can be done using properties of directed graphs. The concept of a strongly connected graph can be formally defined as:

Definition 1. *strongly connected graph:* *a graph in which every node is reachable from every other node.*

Note that Tarjan's algorithm can find the strongly connected nodes in a directed graph in $\mathcal{O}(|V| + |E|)$. This provides a computationally scalable method of calculation for our meshes (several 1,000 nodes). We then take the time to define a mesh stability graph as:

Definition 2. *stable agility graph:* *a set of nodes and edges that are strongly connected but do not include the failure state.*

The stable agility graph gives a space a policy can search over with no concern over failing. Additionally, the strongly connected property insures the reachable space will not contract. If the agility of the policy is measured by the reachable space, then the agility of the switching policy will be stable.

3.5.4   Metrics for Mesh Connectivity

As previously discussed in Section. 3.5.1, finding solutions in the mesh is dependent on initial conditions. We present an analytical solution for simple subset of reachable spaces. The previous Section considered the step length a continous variable. We can discretize the space by creating bins that contain a range of steps. If we want to discretize the space between λ_{min} and λ_{max} with resolution $\delta\lambda$, we can define a set of of m bins. The number of bins are defined as:

$$m = \lceil \frac{\lambda_{max} - \lambda_{min}}{\delta\lambda} \rceil.$$

$B_{group} = bin_1, bin_2, ..., bin_m$. Remember that each node, X has an associated step length λ_X associated with it, because it is the point of double support. The bounds of the nth bin are defined as follows:

$$bin_n = \{X \mid (\lambda_{min} + (n-1)\delta\lambda) < \lambda_X < (\lambda_{min} + n\delta\lambda). \tag{3.15}$$

The binning allows us to group areas of our state space in functionally equivalent groups. Our problem statement only cared about where we placed the feet of the walker. Remember, all nodes place the walker's feet only on the ground; otherwise it is considered a failure state. The bin then provides a variety of initial conditions and controllers which will yield the same step length (to the resolution we specify with $\delta\lambda$).

Once we have placed all the nodes into bins, we utilize a distance metric between an individual node, N, and a individual bin, B. This allows us to see how well connected the node and bin are.

Definition 3. *node-bin distance:* *the metric distance between a node, N, and a bin, B. We write the bin distance as $d(N, B)$ and define it as the shortest number of steps to*

reach node N', which is contained in bin B.

We can then rate the connectivity of the bin, examining all the connections of the nodes contained in the bin. We define the node-bin degree as follows:

Definition 4. *bin degree: a bin B in a set of bins, B_{group}, has a bin degree of D. The bin degree is to represent how well connected a bin is to its neigbors. A low bin degree means bin is very well connected to its neighbors. This is formally written as:*

$$D = \max_{\substack{N \in B \\ B' \in B_{group}}} d(N, B')$$

3.5.5   Solving Foothold Avoidance

As can be seen in Fig. 3.8, the area between 0.38m and 0.48m is well filled in for agility. Here we examine the solution for a mesh which has been binned with λ_{min} of 0.38m and λ_{max} of 0.46m. To illustrate how the maximum and minimum step length affect the passible terrain, we will assume that the bin resolution $\delta\lambda$ is arbitrarily small. To simplify analysis we also assume that the bin degree is 1. This allows our analysis to remove any dependence on initial condition.

The area in blue shown in Fig 3.11 illustrates the runway and gap lengths for which a solution can be found. When the runway is zero (initial foot placement is on the edge of the gap), the maximum step length sets the maximum passable gap. As the robot moves further from the gap, there is an awkward region before the gap where the robot cannot put down a foot. The robot cannot place a foot smaller then λ_{min}, so the effective gap becomes $d_{runway} + d_{gap}$. This represents the downward slope of the triangle as the runway lengthens.

Once there is sufficient space between the robot and the gap, the robot may place a foot before stepping over the gap. This solution is represented in green shading. Notice
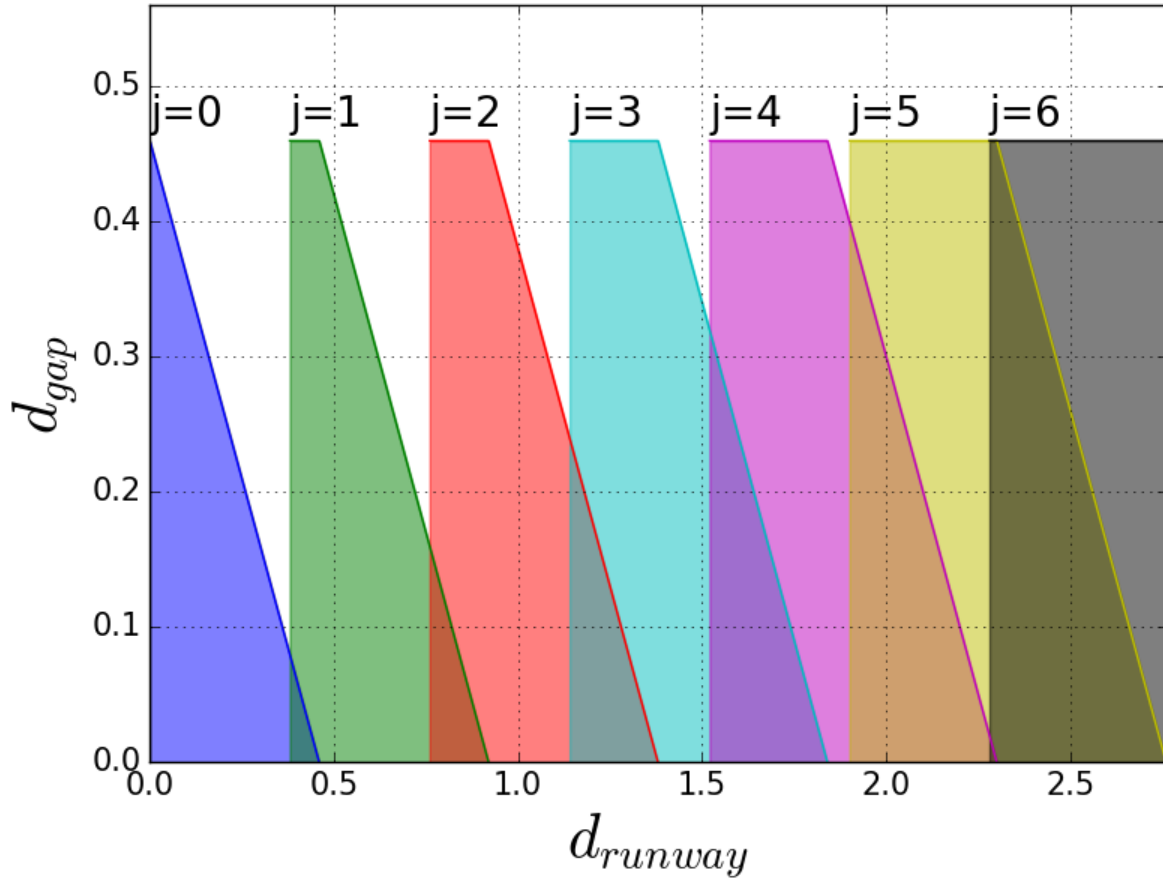
Figure 3.11: This figure depicts the solutions to the problem presented in Section 3.4.3. The d_{gap} is the gap where no footholds can be placed. The d_{runway} is the distance which robot can place steps before the gap. The variable j siginifies the number of steps placed before crossing the gap.

that the passable space changes slightly. Here, the ability to take a short or longer step before the gap allows the robot to modulate the place from which it takes a gap-crossing step. This can be seen as the flat top of the green area. The width of this maximum gap crossing is λ_{min} and λ_{max}.

Note that as more steps are added between the starting position and the gap, the passable terrain becomes larger. Note, also, that if there are j steps, the shortest runway possible would be $j * \lambda_{min}$. The longest runway possible while taking only j steps is $j\lambda_{max}$. For this range of runways the robot can place the jth foothold exactly before the

edge of the gap. This allows the robot to cross a maximum gap of λ_{max} for all of these runways. This feature is represented by the widening plateau of each step area.

As the plateaus widen linearly with the number of steps, solution spaces overlap. For example, the areas with green and red filled in, signify solutions that can be found by taking two or three steps. The more steps are taken the more this overlapping area increases; eventually it fully fills the space for gaps less then λ_{max}. The number of steps where the space is fully filled is $j_{critical}$:

$$j_{critical} = \lceil \frac{\lambda_{min}}{\lambda_{max} - \lambda_{min}} \rceil. \tag{3.16}$$

General Solution

We believe the general solution (bin degree >1) of finding a solution path is a variation of the knapsack problem (NP-complete). This is because each foot-placement, p_j, is simply the sum of previous step length, λ_i:

$$p_j = \sum_j \lambda_i + p_0 \tag{3.17}$$

If we assume a solution exists with j finite steps before the crossing of the gap, the following analysis allows us to draw an equivalent. The constraint that the j step not fall into the gap can be written as:

$$p_j \leq d_{runway}. \tag{3.18}$$

The second half of this problem (walking after the gap) can be succinctly written as:

$$p_{j+1} \geq d_{gap} - p_j. \tag{3.19}$$

Rewrite the Eq.3.18 in terms of the steps taken as:

$$\sum_j \lambda_i \leq d_{runway}.$$ (3.20)

The gap clearance constraint in Eq.3.19 can be written as:

$$\lambda_{j+1} \geq d_{gap} - \sum_j \lambda_i.$$ (3.21)

We can consider Eq.3.20 the weights that must fit into the knapsack, not exceeding its capacity. The knapsack problem generally gives a reward using each weight (or taking each step, in this case), one is trying to maximize. Here we can consider extra space between the gap and step p_{j+1} (step that clears the gap)- as the reward, then Eq. 3.21 can be considered the minimum reward expected. Note that the knap sack problem can be solved in pseudo-polynomial time with dynamic programming. Future work by our lab confirmed solutions where possible, using A* [40].

3.5.6   Solving Foothold Selection

Here we present the solution to the foot hold selection problem presented in Section 3.4.4. The performance of the mesh in solving this problem gives us a measure of how agile the mesh is. We approach the problem as a Markov decision process, with the state S being represented as the robot state X, and the desired foothold λ_d:

$$S = \{X, \lambda_d\}$$

.

We consider the desired foothold to be stochastic process which is distributed in the agile space considered in the foothold avoidance problem:

$$P(\lambda_d) = \text{Uniform Distribution}(0.36m, 0.46m).$$

We then consider the action to be selecting a controller ξ for the subsequent step. This allows us to write a reward $R_a(S)$ equivalent to the cost function presented in Section 3.4.4:

$$R_\xi(X_0, \lambda_d) = -(G(X_0, \xi) - \lambda_d)^2. \tag{3.22}$$

We then search for an optimal policy $\Pi(s)$ that minimizes the expected stepping error, $V(s)$:

$$\Pi(X_0, \lambda_d) = \operatorname*{argmax}_{\xi} R_\xi(X_0, \lambda_d) + \sum P(\lambda_d')\gamma V(X', \lambda_d'). \tag{3.23}$$

The expected reward for the optimal policy can be written as:

$$V(X_0, \lambda_x) = R_\Pi(X_0, \lambda_d) + \sum P(\lambda_d)\gamma V(X', \lambda_d'). \qquad (3.24)$$

We then solve this problem with value iteration [42]. This is done by updating the expected reward, V_i, on the ith iteration as:

$$V_i(X_0, \lambda_x) = \max_\xi R_\Pi(X_0, \lambda_d) + \sum P(\lambda_d)\gamma V_{i-1}(X', \lambda_d'). \qquad (3.25)$$

The results of this optimization are shown in Fig. 3.12 and Fig. 3.13. The relatively small mesh size of 195 points was easily computable on a personal desktop computer. The value iteration converged to a solution after only 100 iterations. Note that the stepping error was largely symmetrical in Fig. 3.12, so we thought it would be more succinct to present the stepping error with absolute magnitude. Note also that the 100% confidence interval means that a bin set degree of 1 can be created as presented in Section 3.5.4. As the bin set degree of 1 is very restrictive, the confidence interval gives us a statistical metric for performance. The confidence interval required really depends on the exact application for foothold selection.
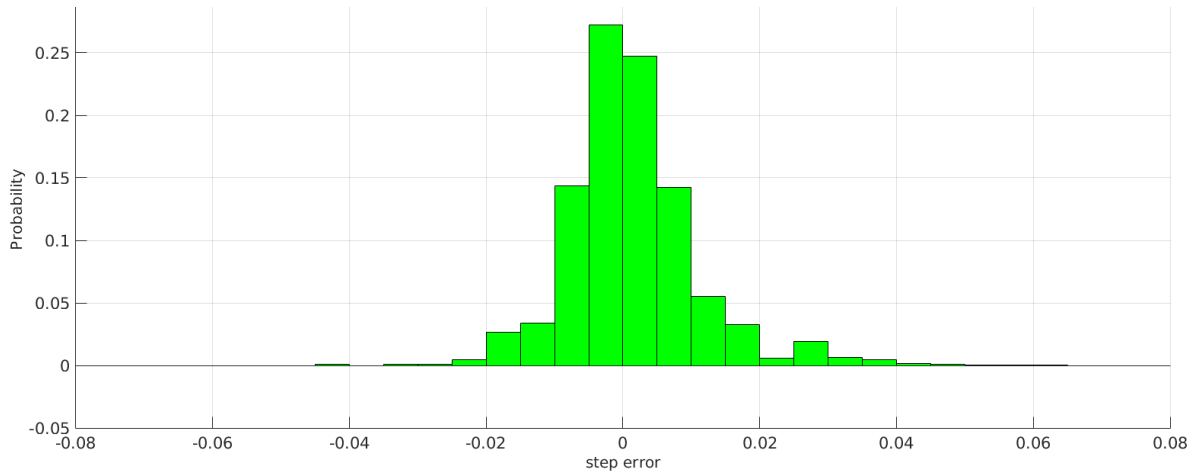
Figure 3.12: This figure shows the probability for each range of stepping error. This discretely approximates the probability density function for the error.
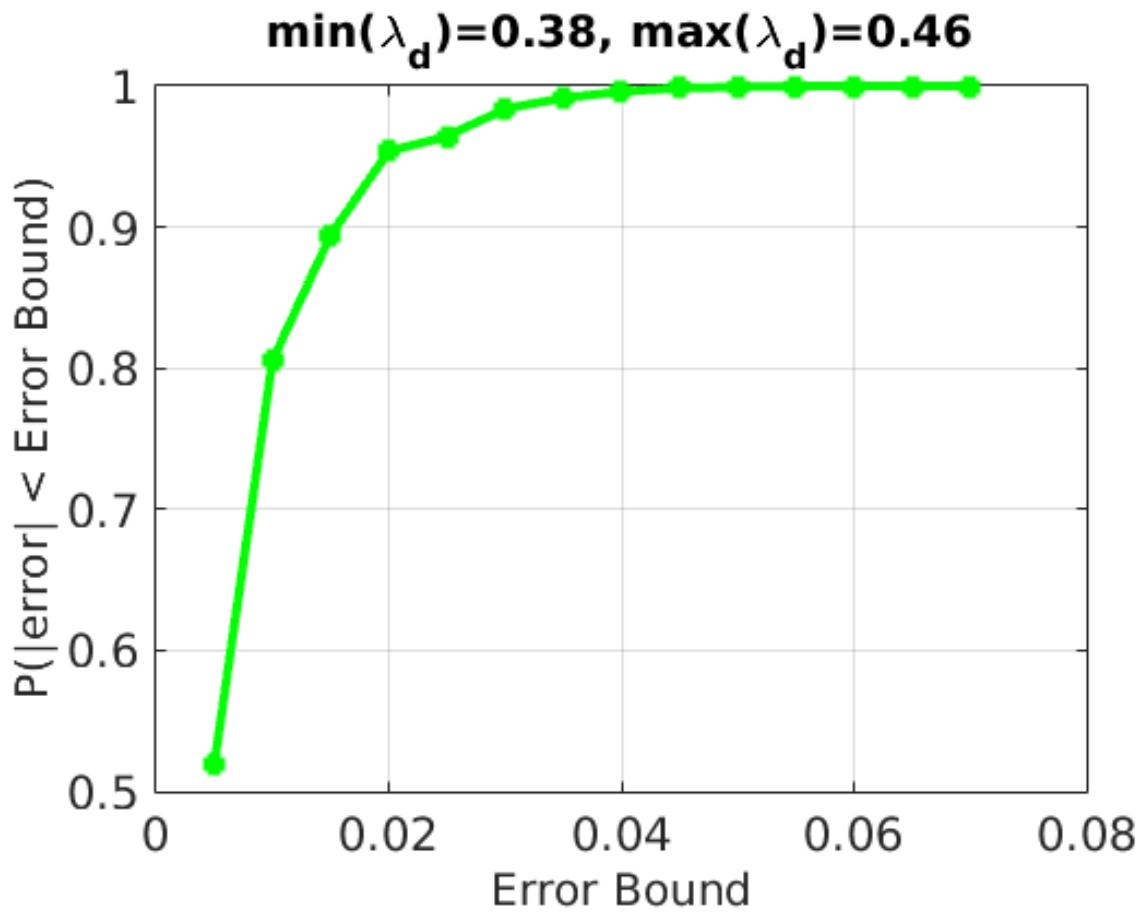

Figure 3.13: This shows the cumulative probability density stepping error for an optimal switching policy that minimizes step error. Note thatthe stepping accuracy is quite high, with a 95% confidence interval of 2 cm. This is with a leg length of 0.8m.

3.5.7   Agility Conclusions

Note that in this chapter, we were able to show extend the energy efficient controller (COT 0.2) performing both accurate foot placement and obstacle avoidance. We create a switching strategy for a biped model to vary its step length by 10% of its leg length while maintaining an accuracy of 2.5% (95% confidence). As the difficulty in hitting a step length is likely proportional to the variability in step lengths, we believe that a more apt comparison for agility performance is:

$$Agility_{placement} = \frac{\sigma(\lambda_d)}{\sigma(\lambda - \lambda_d)}. \tag{3.26}$$

The numerator represents the standard deviation of the desired steps, and the denominator represents the standard deviation of the stepping error. In this way the difficulty of the problem can be balanced with how well the walker performs. For comparison, when humans are given a foot placement challenge they can maintain an accuracy of 6.4% of leg length [37] (desired footholds variability was not reported). We believe that we have presented a good metric frame work that can be applied to dynamic walkers to asses stheir agility.

While we solved a limited case of obstacle avoidance, the structure of passible terrains presented in Fig. 3.11 was confirmed by work done in our lab [40]. The sawtooth form of passible terrain that gradually overlaps was observed. This limited case gives us a plausible explanation for why these features exist in the general case.

Chapter 4

Metabolically Beneficial Exoskeletons

4.1 Augmentation Factor

In designing an exoskeleton to achieve metabolic benefit there are, generally speaking, two main criteria that affect the metabolic energy consumption of the operator. These two factors are the mass of the exoskeleton, and the amount of power the exoskeleton provides. A heavier exoskeleton is a burden on the operator, and a more powerful exoskeleton can help the operator more. This relationship is described formally by the augmentation factor, as devised by Mooney et al. (see [11]). This relationship makes clear that the mass of the exoskeleton matters significantly.

Augmentation Factor can be thought of as the balance between power supplied and mass added. The first term of the equation focuses on the effect of power provided by the exoskeleton based on previous ankle studies [43] [44]. We refer to this first term as the Augmentation Power, or AP. The other half of the equation focuses on the detriment of mass to the user based on a study that examines the effect of large loads on people [45].

The second term we call the Power to Carry henceforth abbreviated as PC.

$$AF = \underbrace{\frac{p^+ - p_{dist}}{\eta}}_{AP} - \underbrace{\sum_i \beta_i(v) m_i}_{PC} \tag{4.1}$$

4.1.1   Power to Carry

The Power to Carry term explains the need for lightweight exoskeletons. The values Mooney et al. used are based on data from Browning et al. [45]. This data is for large masses (4-16 kg) but most metabolically beneficial exoskeletons have been in the 1-3 kg range. The weight and walking speed selected are appropriate for studying obesity, but leave a gap in data for light and fast exoskeletons. Our data is meant to fill this void and inform the development of fast, lightweight exoskeletons.

In keeping with this mindset, there have been a few researchers who have pursued lightweight exoskeletons for metabolic benefit during walking at speeds slower than 1.5 m/s. Malcom et al. [44] and Sawiki and Ferris [46] utilized tethered pneumatic tendons to create exoskeletons that weigh near 2.4 kg. Furthermore, Sawiki and Ferris hold the record for producing 25 W of positive mechanical power [47]. Another lightweight exoskeleton using a purely mechanical device was developed by Collins et al. (see [48]); achieved metabolic benefit over a small population. These studies have not focused solely on the effect of mass on the operator's metabolic energy consumption, though. Thus, it is somewhat difficult to separate the benefit the device provides through its assistive power from the burden of carrying the weight of the device.

One study that has focused solely on the effect of mass on a human's metabolic energy consumption during ambulation is that of Browning et al. (see [45]). They study the effect of mass at the waist, thigh, shank, and foot, but study only two different masses. They conclude that the effect of added mass on metabolic rate increases with distance

from the waist, and with increasing mass, but were only able to see a linear effect with respect to mass. Furthermore, Browning presents data only at a single walking speed. These limitations lead to a lot of assumptions about how humans react to carrying weight while walking, that may not necessarily be true. Furthermore, since it is easily seen that the human gait changes as humans go from walking to running, extrapolating Browning's results to estimate the effect of mass on metabolic rate during running is questionable at best. Yet estimating the effect of mass on metabolic rate is key to designing devices that can aid humans during ambulation at speeds greater than walking.

Here, we present evidence that the effect of added mass is a complex function of location, mass, and velocity. Furthermore, the metabolic impact of added mass is directly required to calculate the Augmentation Factor as defined by Mooney et al. (see Mooney et al. 2014). The location variable in the augmentation factor equation has previously been described by a linear function that depends only on location. This study will provide the data necessary to show the effects on metabolic rate of humans at multiple locations, varying mass, and varying velocity. The goal of this study is to show that the effect on metabolic rate of adding mass at different locations on the leg is in fact a more complex function than previously described.

4.1.2   Augmentation Power

For a correctly designed exoskeleton, the augmentation power should be the largest positive number possible. As a reminder, mechanical power is τ_i torque at ith joint times ω_i rotational speed. These equations assume that the torque is being applied at a reasonable time and magnitude. The η is an exoskeleton efficiency that is observed for ankle torques [43]. One can hypothesize that the exoskeleton can reach a point of applying more torque than the person needs. At this point we may see diminished benefit

or even a detriment to the human's performance. The maximum power supplied to a person walking is 30 W [47], so it is an unobserved human response.

The positive power of an exoskeleton, p^+, is assumed to replace muscle activation. The p_{dis} is the dissipated power and is a piecewise function relating positive and negative energy. One should be aware of the difference between dissipated energy and negative energy. (Refer to 4.4 for exact specifications.) This is an important distinction that allows for the explanation of passive exoskeletons that are metabolically beneficial, such as those created by Collins et al. [48].

$$p^+ = \frac{\int_0^T P_{\text{exo}}(t)dt}{T}, \text{ for } P_{\text{exo}}(t) > 0 \tag{4.2}$$

$$p^- = \frac{\int_0^T P_{\text{exo}}(t)dt}{T}, \text{ for } P_{\text{exo}}(t) < 0 \tag{4.3}$$

$$p_{dist} = \begin{cases} p^- + p^+ & p^- < -p^+ \\ 0 & else \end{cases} \tag{4.4}$$

Our preliminary investigations into the effect of Augmentation Power are presented in Section 4.6.

4.2 Added Mass Study

The relevance of added mass to locomotion has a broad set of implications for robotics, prosthetics, and orthotics. There is an ongoing challenge in robotics to create agile and energy efficient robots. Understanding how added mass affects human cost of transport can inform and inspire design choices for mass distribution in legged robots. Roboticists should carefully consider that the total mass added by wearing a device is only

part of the consideration in design: choice of distribution of this mass along a human body has important consequences. Additionally, robotic prosthetics are recently becoming commercially available. Fatigue and unnecessary strain in prosthetic users is well documented, and something that could potentially be alleviated with more optimal mass placements. In addition, robotic exoskeletons designed to augment human performance can be optimized only if one first understands the effects of added mass. The only exoskeletons to aid humans have operated, to date, at walking speeds. We believe that there is still a lot to learn about the effects of mass and its distribution on people as they run.

The tests were conducted by strapping various weights to human subjects at the foot, ankle, top of the shank, above the knee, and below the hip. The subjects then walked and/or ran on a treadmill at four different speeds: two walking speeds and two running speeds. During each of these trials the metabolic rate of the subject was recorded.

4.2.1   Experimental Method for Added Mass

Leg Loads

The masses of the weights were chosen to be relevant to the design of lightweight exoskeletons. We used three weights at each location in order to probe nonlinearities in the effect of added mass. Rather than loading the minimum and maximum tolerable loads at each segment or location ([45]), we used a closer grouping of weights at a given location. At the foot and ankle locations we used 0.45, 0.91, and 1.36 kg loads which are similar in masses to lower-leg prosthetic devices [49]. We used 1.36, 1.81, 2.27 kg loads at the shank and lower thigh locations. At the high thigh we used 2.27, 2.72, and 3.18 kg loads. The weights were placed on the subject by using tape to wrap or attach therapy weights to the foot, shank or thigh segments. Duct tape was used to secure the

weights in place when necessary. For all shank and thigh loads, the weights were wrapped around the the subject's leg at the location designated. (Refer to Fig.4.1.) The possible locations for the shank were at the ankle and directly below the knee. The two locations for the thigh were directly above the knee and the highest point on the thigh.

mid foot	lower shank	upper shank	lower thigh
50%	15%	75%	15%

Table 4.1: The placements of weights for this study. Note that for the percentage of segment length measuring 0% is distal and 100% is proximal. For example, 0% on the foot would be a weight placed at the toe.

Speed Selection

Subjects completed a baseline walking trail each day at 1.0 m/s followed by walking trials at 1.25 m/s and 1.75 m/s. Running trials were completed at 2.0 m/s and 2.75 m/s. These speeds were chosen to cover a wide range of speeds in order to capture the metabolic effects over the largest space. Furthermore, the four speeds are split such that two enforce a walking gait, while two enforce a running gait.

Experimental Protocols

Ten healthy subjects (eight male, two female, 26.1 ± 3.1 years, 77.2 ± 11.9 kg, 1.78 ± .07 meters) volunteered for this study. All 10 subjects gave written informed consent to participate in this study. Subjects completed a total of 52 tests comprised of both walking and running. The walking tests were at 1.25 and 1.75 m/s. Running tests were at 2.00 and 2.75 m/s. The trials began with no-load walking and running trials at each speed followed by the loaded trials. The loaded trials consisted of a set of three weights at four different locations. The loaded trials were chosen in a random order of location, weight, and speed. Once the location was chosen for the first trial, a mass was chosen at

random out of the three possible weights. The subject would then complete a randomly selected order of the four possible speeds with that weight before a new weight was chosen at the same location. The subject completed all tests at the selected location before a new location was chosen. This selection process was repeated until all location sets were completed. Each subject was tested with weight at four of the five possible locations. Each test lasted between 3 and 7 minutes to allow the subject to reach a steady state metabolic rate.

An institutional review board gave approval for all experimental procedures and study criteria. All testing took place on a commercial grade treadmill (Freemotion 860). Treadmill speed was verified with reflective markers to within $\pm$ 0.05 m/s.

Data Collection

In order to measure the cost of adding mass to the subjects during walking and running we measured the rates of oxygen consumption and expired gas analysis using a portable metabolic system (CardioCoach, Korr Medical Technology). Prior to trials beginning, subjects performed a baseline walking test at 1.0 m/s. This baseline test was performed each day of testing before subjects completed any trials.

Note that in our data processing we calculated the baselined metabolic by having the subjects walk at 1 m/s at the start of each day. All subsequent tests during that session were subtracted by this baseline conditon. We refer to these values as "baselined values."

During the walking and running trials, the rate of oxygen expiration (averaged over 15 second intervals) was observed to confirm the subjects were at steady state during each trial. The rate of oxygen expiration during the steady state was then averaged for comparison to other trials. The metabolic effect data for each trial was adjusted by subtracting the baseline metabolic effect for that day. This effectively normalized the data to account for the inconsistencies in human metabolic energy consumption that

occur on a day-to-day basis. Furthermore, since we are interested in determining the effect of mass on a human's metabolic rate, we are actually interested in the difference between the rate of metabolic energy consumption during each trial with mass and the rate of metabolic energy consumption during the no-load trial at the same velocity. As such, we further normalized each trial by subtracting the baseline adjusted metabolic rate measured for the no-load trial, at the corresponding velocity.

Extracting Metabolic Effect

The main objective of this study is to begin to quantify the relationship of metabolic effect to mass added to the legs across three variables: velocity, amount of mass, and location of mass. In the remainder of this section we study each of these three relationships individually. We start by looking at the effect of mass location on metabolic rate, then proceed to the effect of changing ambulation velocity while holding mass and mass location constant, and finally examine the effect of changing mass while holding location and ambulation velocity constant.

We consider the metabolics of a person P, as a function of the added mass, M, added mass location, L and forward speed, V. We write this as:

$$P_L(M, V)$$

.

Because our Augmentation Factor focuses on the change from the unloaded condition, we always compare the metabolics of a person to the unloaded condition. We commonly call it the no-load value. For a particular subject, there was only one no-load condition taken in the whole study. Note that we use the notation 0 when no added mass is placed

on the person. The no-load conditon is then written as:

$$P_L(0, V)$$

We calculate the Power to Carry, PC_L, of a person then as the difference between their affected condition and their no-load condition at the same velocity. We explicitly define the power to carry as:

$$PC_L(M, V) := P_L(M, V) - P_L(, 0, V). \tag{4.5}$$

4.3 Metabolic Effect Scaling with Mass

Note that Browning et al. [45] found linear relationships between added mass and metabolic effect on the user. The fact that we only tested three masses and the high amounts of noise did not allow us to test for high polynomial terms. In the future, we hope to test higher masses to both aid in polynomial fit testing and give a higher signal-to-noise ratio.

4.3.1 Midfoot Mass

The midfoot was studied with five subjects, as we expected a much cleaner signal and did not expect to need large numbers of samples. The bilateral loads tested were 0.9 kg, 1.8 kg, and 1.4 kg. As can be seen in Fig.4.2, The midfoot was found to have a statistically signifant linear trend of 19.9 Watts per kg of added mass at 1.25 m/s walking (p = 2.41e-05). Note that Browning et al. [45] found an effect of 14.8 W/kg when placing weight at the foot's approximate center of mass. This location is more anterior and distal than the midfoot placements we used. We did not find a statistical difference between

our result and those reported by Browning et al. (p = .134). Fig. 4.3 shows the faster walking speed of 1.75 m/s. The ordinary least squares found the effect of 23.3 W/kg (p = 4.70e-05). This was also not statisticlly signifcant from the values reported by Browning et al at. 1.25 m/s walking (p = 0.052).

The running effects are depicted in Fig. 4.4 and Fig. 4.4. The running at 2.0 m/s was found to have the statistically significant effect of 36.84 W/kg (p = .003). Note this value was not statistically significantly from the value reported by Browning et al (p = .054). The fastest running speed of 2.75 m/s had the statistically significant effect of 53.2 W/kg (p = .001). The effect of running at 2.75 m/s with mass at the midfooot was statistically increased from the values reported by Browning (p = 0.008).
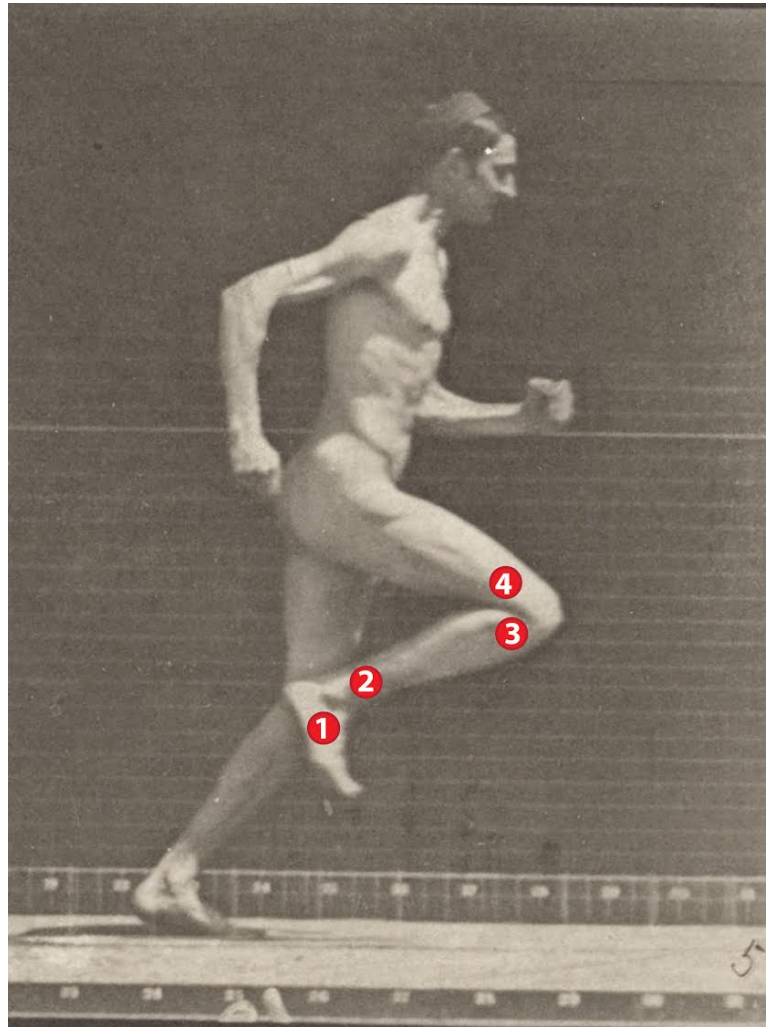
Figure 4.1:   This image by Eadweard Muybridge has an overlay of the mass placements for our study. The four mass placements were 1) foot 2) lower shank 3) upper shank 4) lower thigh. The same mass weight was placed on both legs, at only one spot at time.
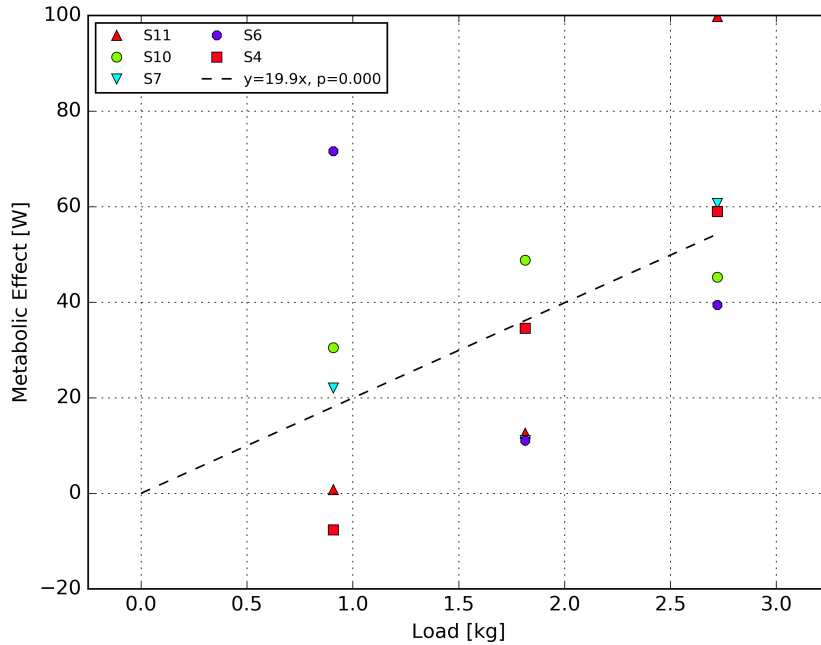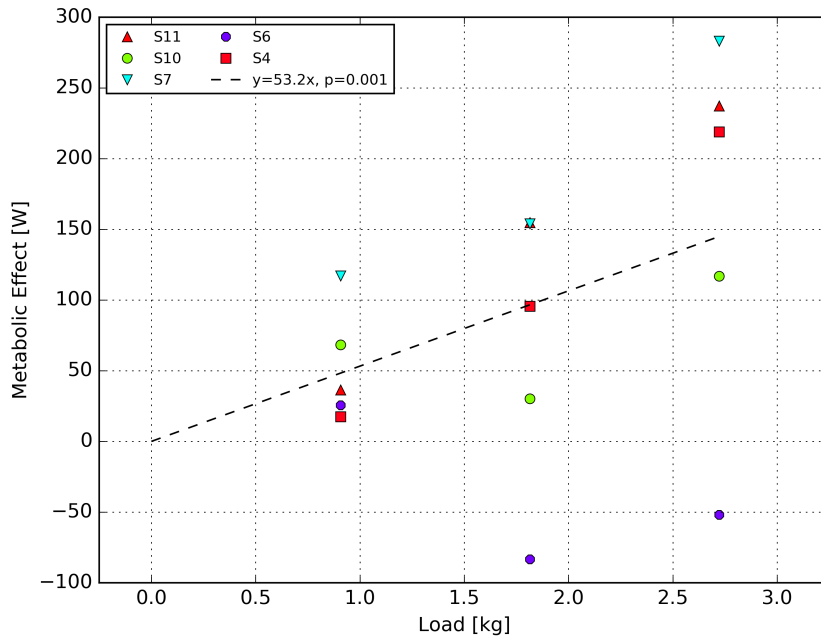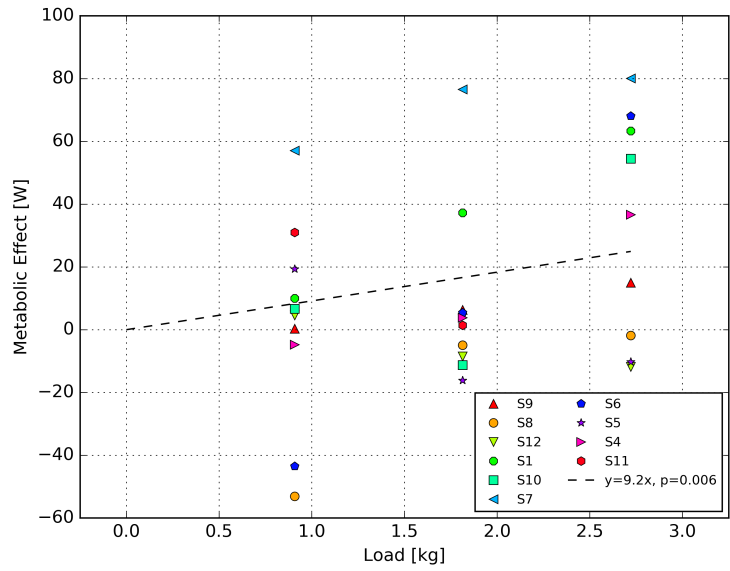
Figure 4.2: The metabolic effect compared to walking at 1.25 m/s. The slope defines the effect of adding orthotic mass. The load is defined as the total weight placed bilaterally. The mass was strapped to the top of the midfoot.
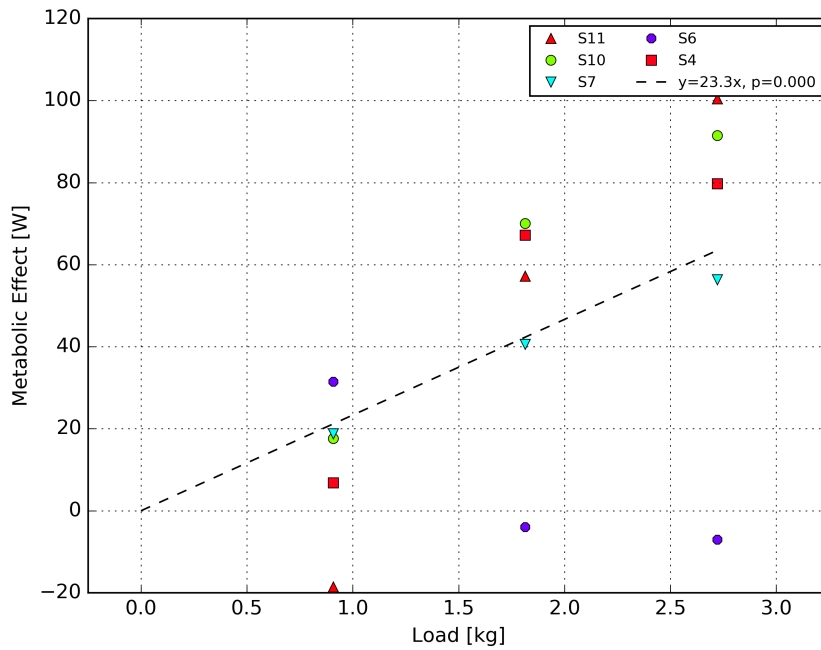
Figure 4.3: The metabolic effect compared to walking at 1.75 m/s. The slope defines the effect of adding orthotic mass. The load is defined as the total weight placed bilaterally. The mass was strapped to the top of the midfoot.

72
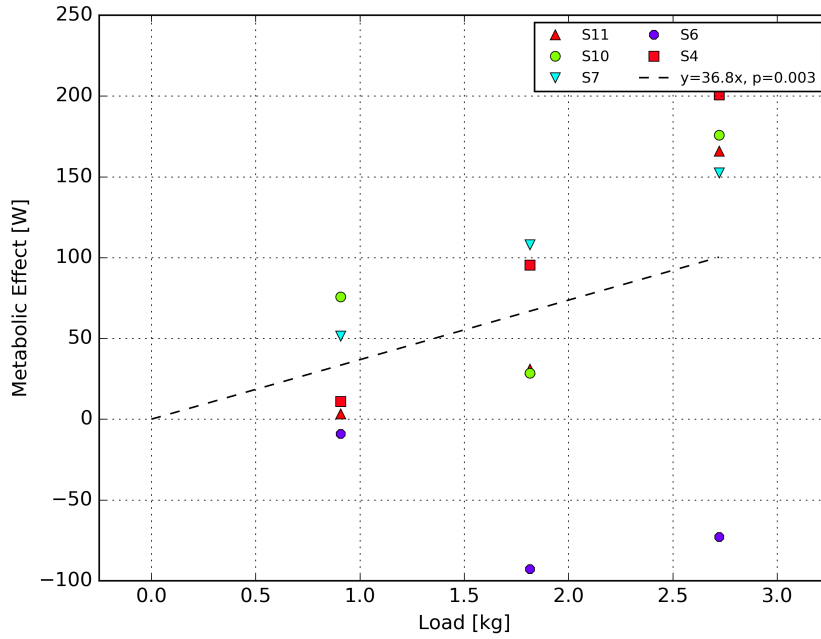
Figure 4.4: The metabolic effect compared to running at 2.0 m/s. The slope defines the effect of adding orthotic mass. The load is defined as the total weight placed bilaterally. The mass was strapped to the top of the midfoot.

Figure 4.5: The metabolic effect compared to running at 2.0 m/s. The slope defines the effect of adding orthotic mass. The load is defined as the total weight placed bilaterally. The mass was strapped to the top of the midfoot.

73

4.3.2   Lower Shank Mass

The lower shank masses were tested with 10 subjects. The bilateral loads tested were 0.9 kg, 1.8 kg, and 1.4 kg. We placed the mass 15% of the proximal distance from ankle to knee joint. As shown in Fig. 4.6a, the least squares fit found a significant fit of 9.2 W/kg (p = .006) at 1.25 m/s walking. The slope was higher but not statistically more significant (p = .26) than the values of 5.62 W/kg at the shank reported by Browning et al. We believe the difference may be due to the different weight placements in the studies. Browning et al. placed weights 55% of the way up the shank in contrast to our 15% placement for "lower shank."

As shown in Fig. 4.6b, the faster walking speed of 1.75 m/s the shank had a cost of 9.38 W/kg (p =.04). Note that ordinary least squares regression is susceptible to outliers in data, and Fig. 4.6b shows two outliers, S4 and S11, at 1.8 kg. We therefore believe more analysis and testing is necessary for insuring an accurate fit to the the regression.

As shown in Fig. 4.7b, for the slower of the running speeds the regression found a statistically significant slope of 23.0 W/kg (p = .0001). Note that this set of data contained an outlier with Subject 7 at 1.8 kg. For the fastest running speed of 2.75 m/s our regression found a slope of 27 W/kg (p = .002). While these slopes imply that the metabolic effect grows with forward velocity, we leave that analysis for a later section.
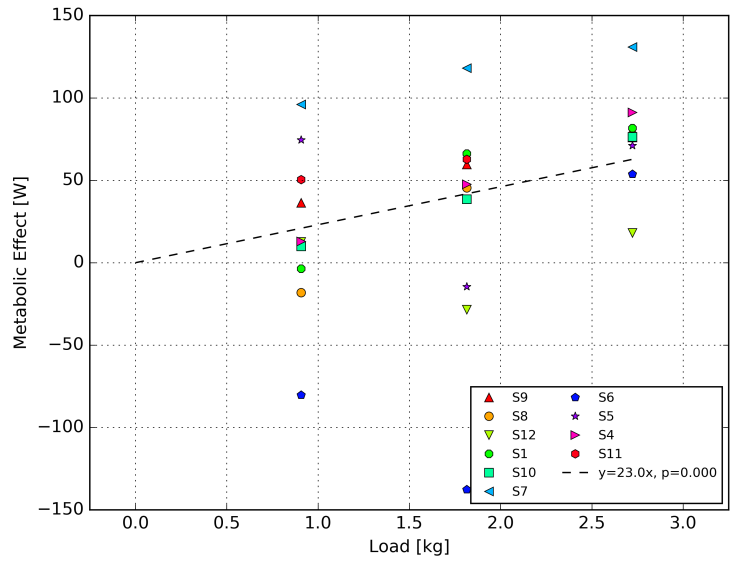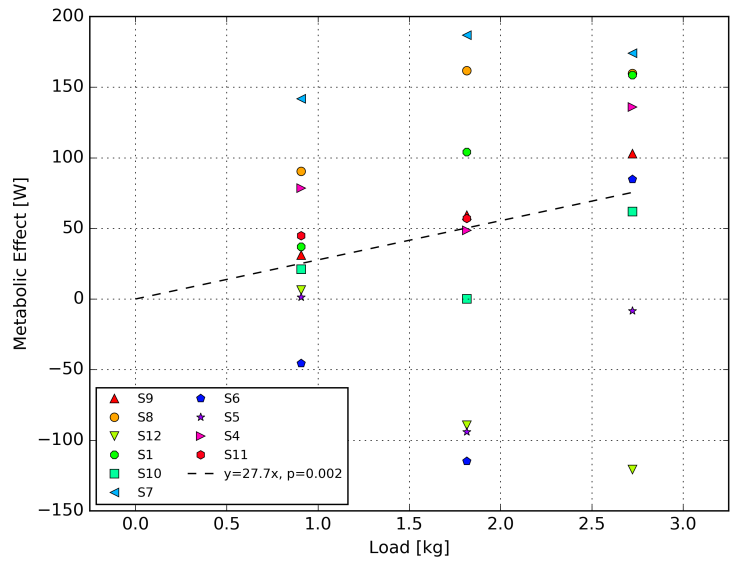
(a) 1.0 m/s walk
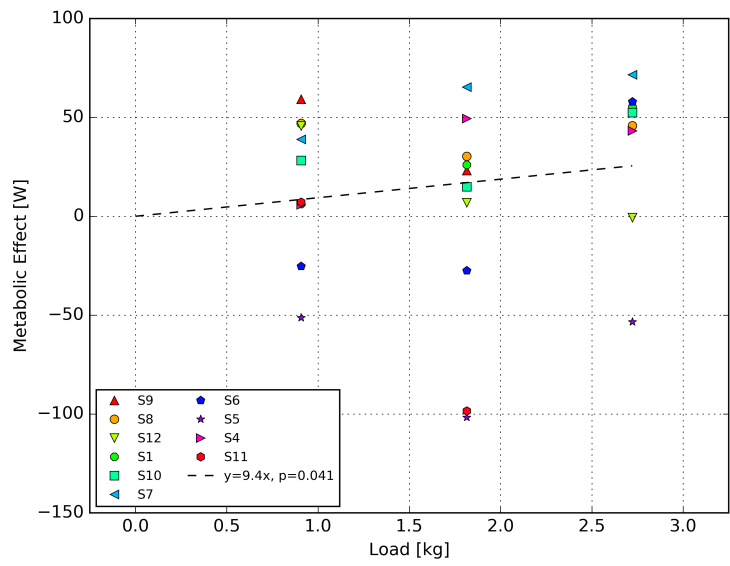
(b) 1.75 m/s walk

Figure 4.6: The metabolic effect compared to when walking at 1.25 m/s (a) and 1.75 m/s (b). Both figures are at walking speeds. The slope defines the effect of adding orthotic mass to the lower shank. The load is defined as the total weight placed bilaterally.

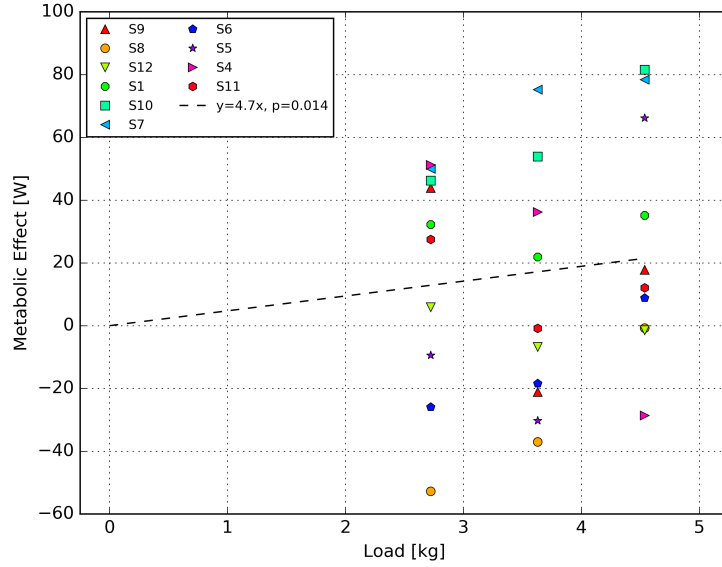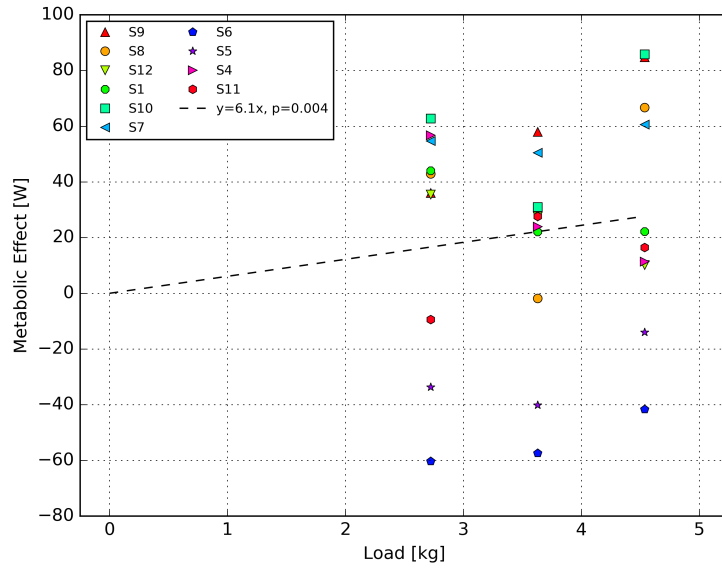(a) 2.25 m/s run

(b) 2.75 m/s run

Figure 4.7: The metabolic effect compared to when running at 2 and 2.75 m/s. Both figures are at running speeds. The slope defines the effect of adding orthotic mass to the lower shank. The load is defined as the total weight placed bilaterally.

4.3.3   Upper Shank Mass

The upper shank mass was tested with 2.7k g, 3.6 kg, and 4.5 kg on 10 subjects. We believe the high loading from the lower shank was more representative of the mass for a powered knee orthotic. Note that the slowest walking of 1.25 m/s (depicted in Fig. 4.8a) shows our statistically significant fit of 4.7 W/kg (p = .014). Note that this was not a statistically significant difference from Browning's reported value of 5.62 W/kg on the shank (p = .62). Our "upper shank" placement was 75% of the height of the shank. In contrast, Browning et al. placed their mass at 55% of the height of the shank, where they estimated the COM of the shank to be.

As seen in Fig. 4.8b, the best fit slope was 6.1 W/kg (p = .004). This modest increase in slope was still not statistically different from 5.62 W/kg (p = .81). As the subjects ran at the lower running speed of 2.0 m/s, the slope became 9.6 W/kg (p = .013). While a larger effect than the 1.25 m/s walking, this was not a statistically significant difference from Browning's shank value (p = .28).

As shown in Fig. 4.9b, when subjects ran at 2.75 m/s the upper shank's effect was estimated at 13.4 W/kg (p = .004). Despite the expected slope being significantly larger than the Browning et al. value, this was not a statistically significant difference (p = .08). As all the estimated fits increased with speed, we suspected that there was a velocity relationship to metabolic effect. The statistical analysis of this relationship is shown in subsequent sections.
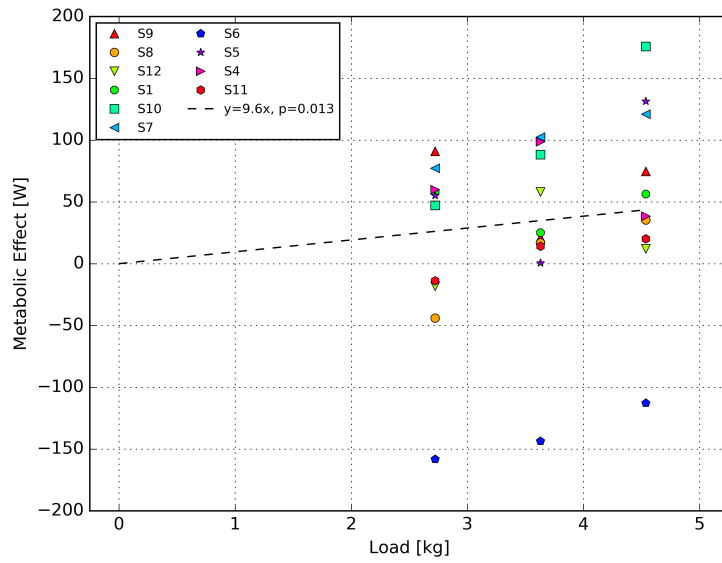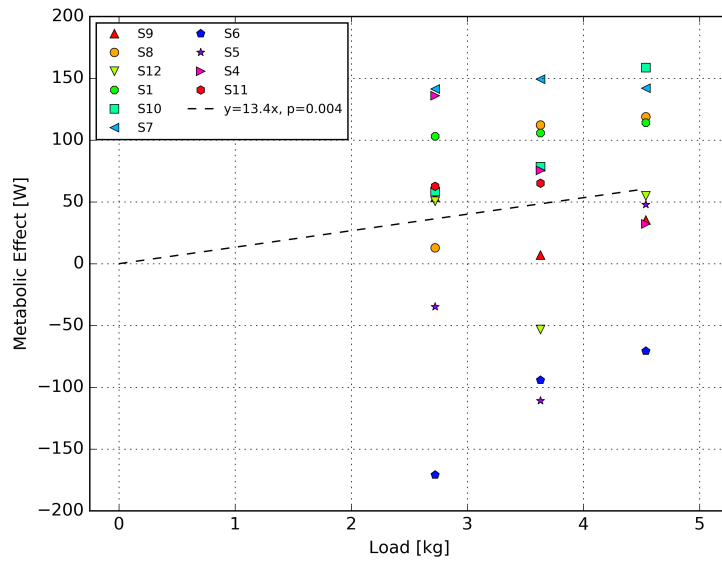
(a) 1.25 m/s walking

(b) 1.75 m/s walking

Figure 4.8: The metabolic effect compared to walking at 1.25 and 1.75 m/s. Both figures are at walking speeds. The slope defines the effect of adding orthotic mass. The load is defined as the total weight placed bilaterally. The mass was strapped to the top of the shank where it would not interfere with the knee joint.

(a) 2.0 m/s running

(b) 2.75 m/s running

Figure 4.9: The metabolic effect compared to running at 2.0 and 2.75 m/s. Both figures are at running speeds. The slope defines the effect of adding orthotic mass to the lower thigh. The load is defined as the total weight placed bilaterally. The mass was strapped to the top of the shank where it would not interfere with the knee joint.

4.3.4   Lower Thigh Mass

We examined the results from mass placements on the lower thigh. Specifically, the slowest walking speed of 1.25 m/s the least squares fit found a slope of 4.8 W/kg (p = .00013). This regression was not statistically different from the the value of 5.55 W/kg reported by Browing et al. for weight placed on the thigh (p = 0.48), At the faster walking speed of 1.75 m/s the regression gave a slope of 8.4 W/kg (p = 4.31e-05). Again, this was not statistically different from the value reported by Browning for walking at 1.25 m/s (p = 0.10).

As can be seen in Fig. 4.11a, our regression found a significant slope of 8.4 W/kg (p=0.0003) for running at 2.0 m/s. In contrast, Fig. 4.10b the fastest running speed 2.75 m/s had a statistically signifcant regression of 13.4 W/kg (p=0.0004).

While our regression was not statistically different from the 1.25 m/s value reported by Browning et al. (p = .131), we did find a statistically significant difference for the fastest running speed of 2.75 m/s (p = 0.024). It is important to remember that our placements were at 15% of the thigh length, while Browning's placements were at 55% of the thigh length. The lack of statistical difference in measurement at slow walking speeds but the presence of a difference at high running speeds, would imply running and/or speed has a important relationship to the effect of added mass. We leave the further investigation into this question until Section 4.5.

Note that the loads used were 2.7 kg, 3.6 kg, and 4.5 kg. Note that the spacing of 0.9 kg between loads limited the information gathered during each test. For example, if the linear regression is correct, then at the slowest walking speed there would be a difference of only 4.32 W between each data point. Our data indicated that the standard error for the means was between as low as 5 W (1.25 m/s walking) and as high as 20 (2.75 m/s running). This large signal-to-noise ratio limited our ability to test the linear assumption

between mass and metabolic effect. We hope to further test the linear assumption by increasing the load to points where quadratic terms would dominate.

The results from the lower thigh appeared to be very similar to those from the upper shank. In subsequent sections we will more closely examine if there was a statistical difference between the upper shank and the lower thigh. These locations are very relevent for the design of knee orthotics.
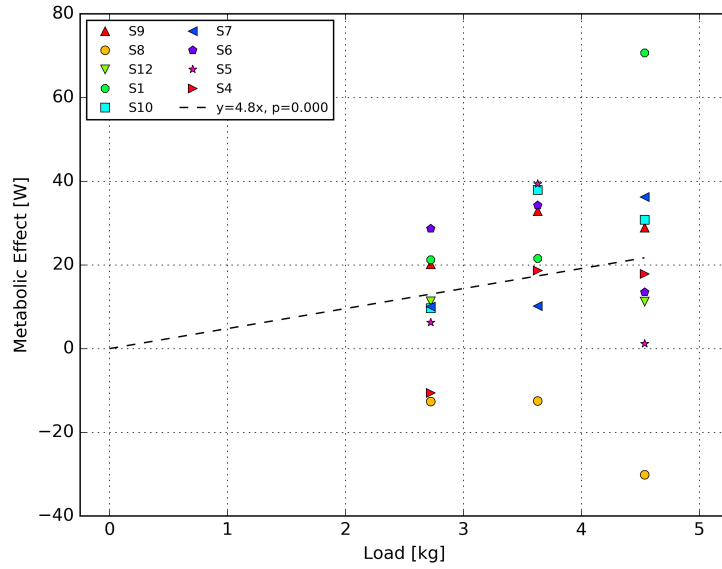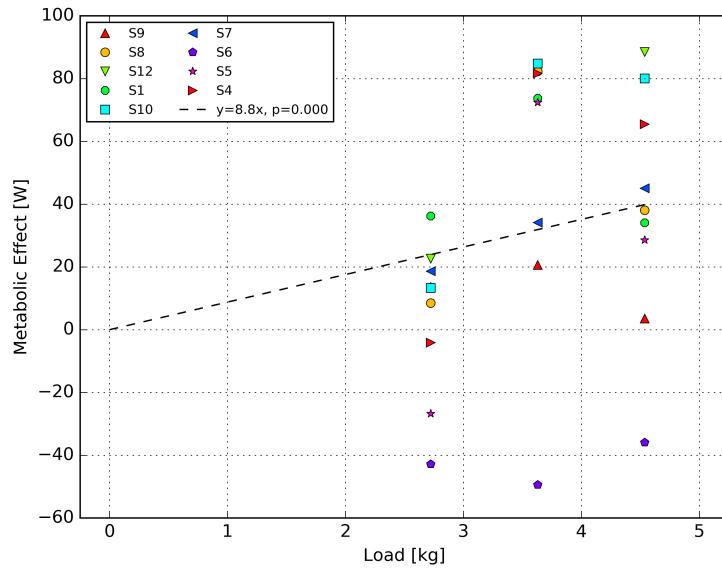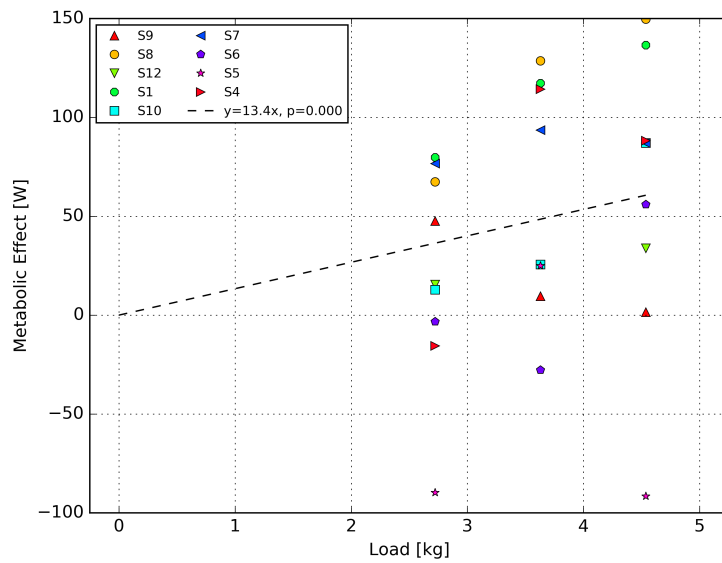
(a) 1.25 m/s
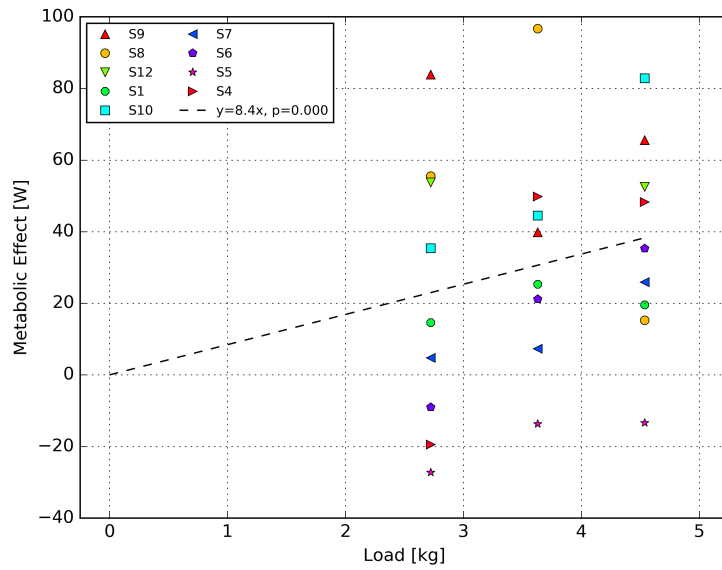
(b) 1.75 m/s

Figure 4.10: The metabolic effect compared to walking at 1.25 and 1.75 m/s. Both figures are at walking speeds. The slope defines the effect of adding orthotic mass. The load is defined as the total weight placed bilaterally. The mass was strapped to the lower thigh where it would not interfere with the knee joint.

(a) 2.0 m/s

(b) 2.75 m/s

Figure 4.11: The metabolic effect compared to running at 2.0 and 2.75 m/s. Both figures are at running speeds. The slope defines the effect of adding orthotic mass to the lower thigh. The load is defined as the total weight placed bilaterally. The mass was strapped to the lower thigh where it would not interfere with the knee joint.
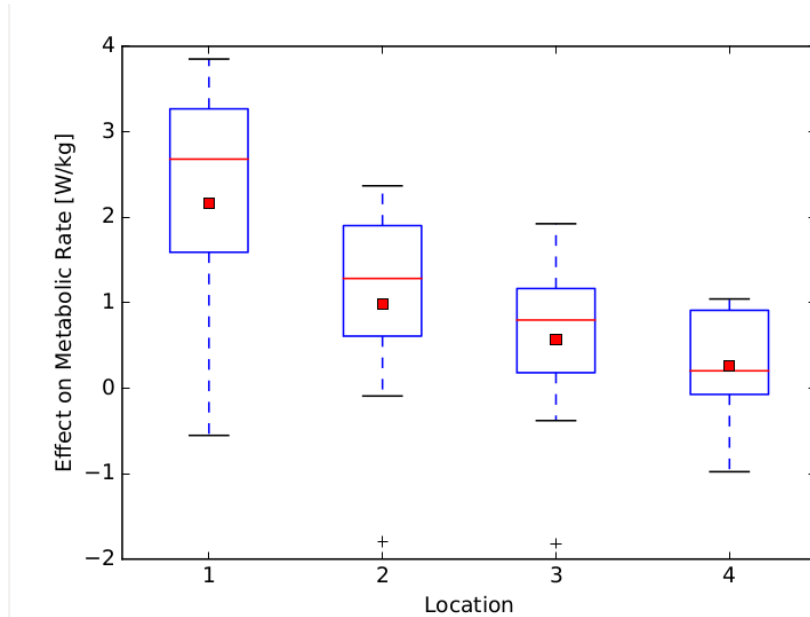
4.4   Distal Mass

Figure 4.12: This figure depicts the human's response running at 2.75 m/s. 2.7 kg mass was evenly distributed between both legs. The mass was concentrated at the following locations: 1) foot 2) lower shank 3) upper shank 4) lower thigh. Above, one can see that the placement of the mass is important to the response of the human. Mass placed distally is a significantly larger burden.

Distal mass, defined as mass applied furthest from the center of the body, has been known to be burdensome to locomotion. As can be seen in Table 4.2, for Browning et al. [45] weight carried closer to the foot caused more of a metabolic burden. Note that while our slowest test speed matched this, our mass placements did not match it. The foot mass placement for Browning et al., shown in Fig. 4.13 was different from that done in this study. We believe that the 14.8 W/kg [45] [11] foot mass represents a point between our Location 1 (midfoot) and Location 2 (ankle).

speed	foot	upper shank	midthigh	waist
1.25 m/s	14.8 W/kg	5.62 W/kg	5.55 W/kg	3.33 W/kg

Table 4.2: The metabolic effect in Watts per kilogram of orthotic. The data is based on Browning et al.[45] and the fit are presented by [11]

speed	midfoot	lower shank	upper shank	lower thigh
1.25 m/s	19.9 ± 3.2 W/kg	9.2 ± 3.1 W/kg	4.7 ± 1.8 W/kg	4.8 ± 1.1 W/kg
1.75 m/s	23.3 ± 4.0 W/kg	9.4 ± 4.4 W/kg	6.1 ± 2.0 W/kg	8.4 ± 1.7 W/kg
2.00 m/s	36.8 ± 10.5 W/kg	23.0 ± 5.1 W/kg	9.6 ± 3.6 W/kg	8.8 ± 2.1 W/kg
2.75 m/s	53.2 ± 12.3 W/kg	27.7 ± 8.2 W/kg	13.4 ± 4.2 W/kg	13.4 ± 3.3 W/kg

Table 4.3: Note that all slopes were P < .05.

Figure 4.13: This figure depicts the mass placement for Browning et al. [45]. Note that the lead weights were placed on the shoelaces as well as on the heel of the shoe. The added mass study presented here utilized therapy weights (vinyl covered bags filled with steel pellets). Due to the higher volume of steel pellets, the weight was fastened to the shoelace section of the shoe with tape.
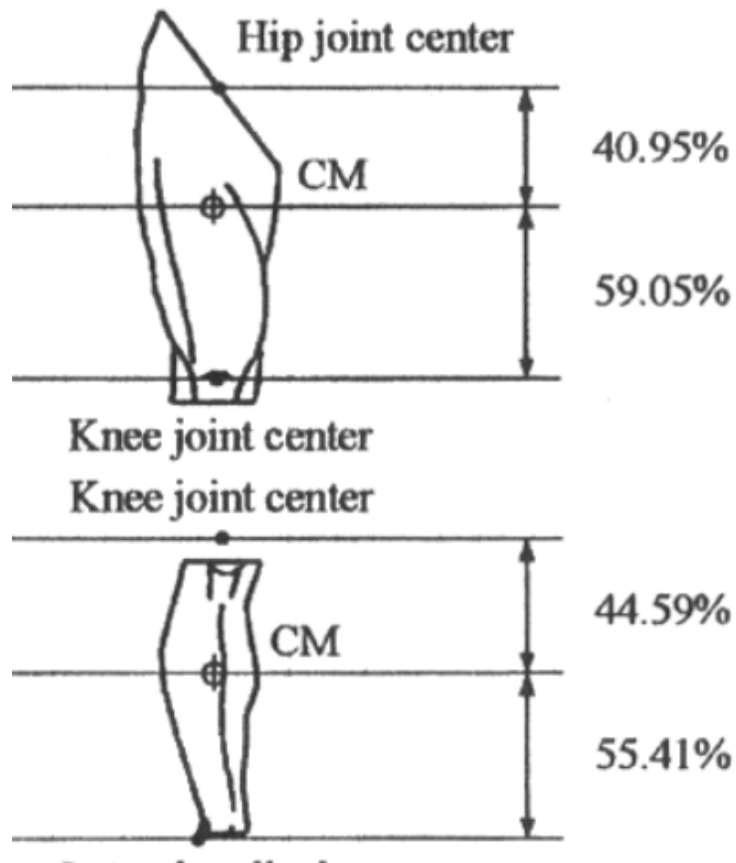
Figure 4.14: This figure depicts the mass placement for Browning et al. [45] on the shank and thigh. Browning et al. placed mass at the estimated CM of the shank and thigh respectively. The center of mass of each segment was based on values published by De Lena [50] The added mass study presented here utilized therapy weights (vinyl covered bags filled with steel pellets). Due to the higher volume of steel pellets, the weight was fastened to the shoelace section of the shoe with tape.

4.5   Velocity Scaling

As Section 4.3 shows, our regressions showed increased metabolic expenditures with forward velocity. Note that variability in metabolic measurements made statistical analysis on the effect of velocity difficult. In this section we look to investigate in more detail how velocity affects added mass.

Intuition guided our expectation that high velocity would increase the cost of carrying mass. We examined the effect of fixed mass with increasing velocity. We selected the largest mass at each joint, which from the previous sections analysis correlated with the largest signal. The standard mean errors for each mass and velocity ranged from as small as ± 2 W to as large as $\pm$ 16 W.
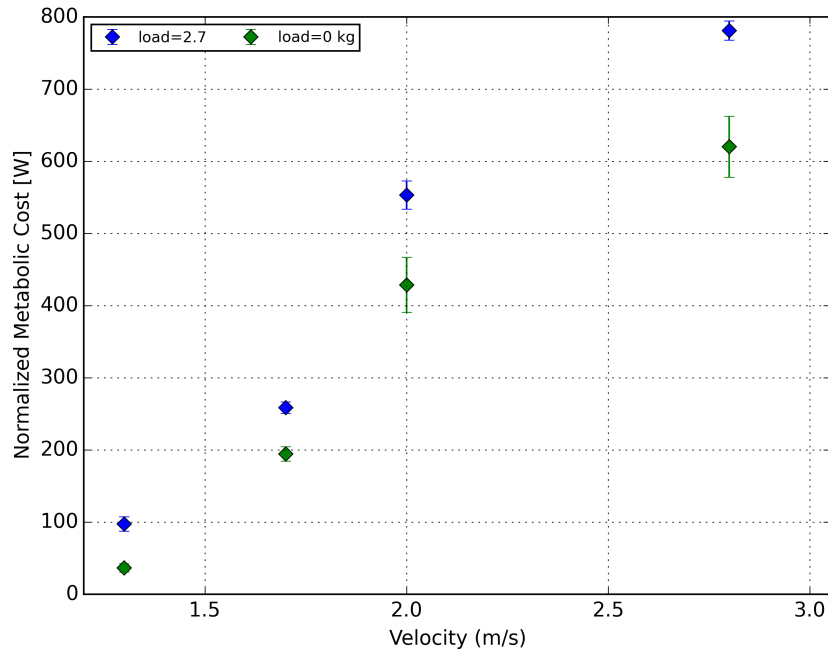
Figure 4.15: This graph shows the expected increasing metabolic expenditure with forward speed. Each data point represents the mean across subjects, and the error bars represent the standard error of the mean. The metabolic cost is normalized by a slow walking baseline value (walking 1.0 m/s). This was done to normalize for variations in resting metabolic rate. The metabolic expenditure increases with forward speed in both loaded and unloaded conditions, as the human must expend more energy to run faster. The gap between the loaded and unloaded conditions appears to be growing with forward velocity. Five subjects were tested under these conditions.
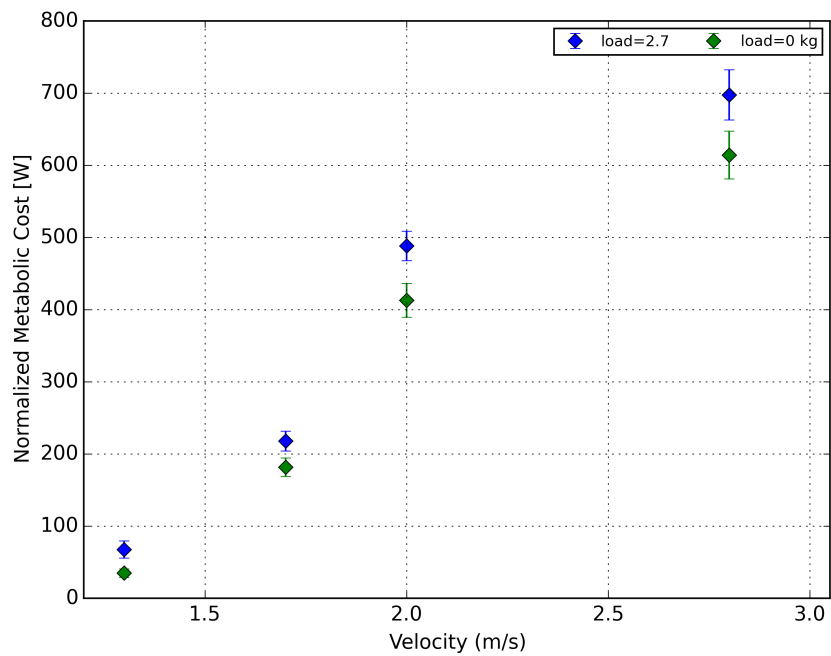
Figure 4.16:   This graph depicts the difference between no load and a load of 2.7 kg placed on the lower shank. Each data point represents the mean across subjects, and the error bars represent the standard error of the mean. The metabolic cost is normalized by a slow walking baseline value (walking 1.0 m/s). This was done to normalize for variations in resting metabolic rate. Notice that the loaded condition cost grows faster than the unloaded condition. Ten subjects were tested at these conditions.

Figure 4.17: This graph depicts the difference between no load and a load of 4.5 kg placed on the upper shank. Each data point represents the mean across subjects, and the error bars represent the standard error of the mean. The metabolic cost is normalized by a slow walking baseline value (walking 1.0 m/s). This was done to normalize for variations in resting metabolic rate. Notice that the loaded condition cost grows faster than the unloaded condition. Ten subjects were tested at these conditions.
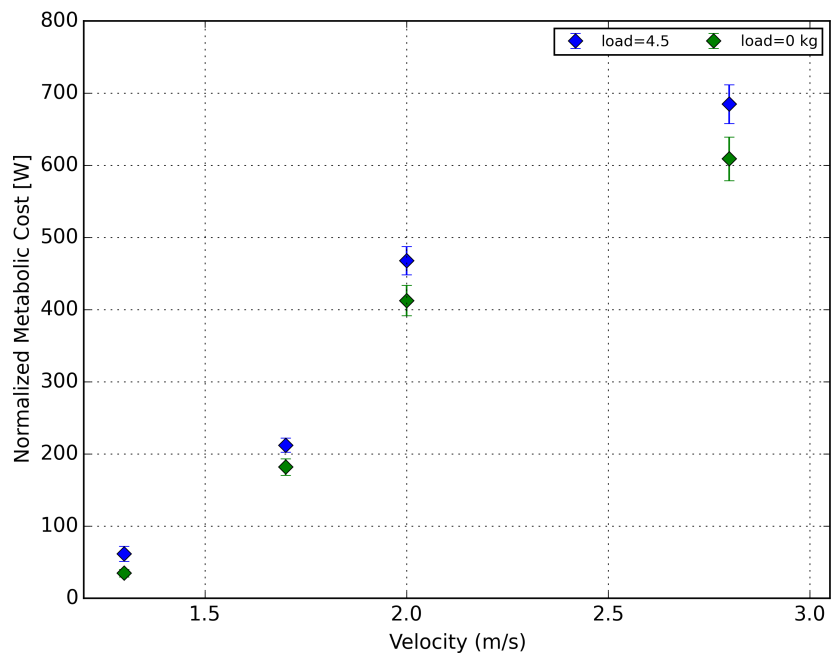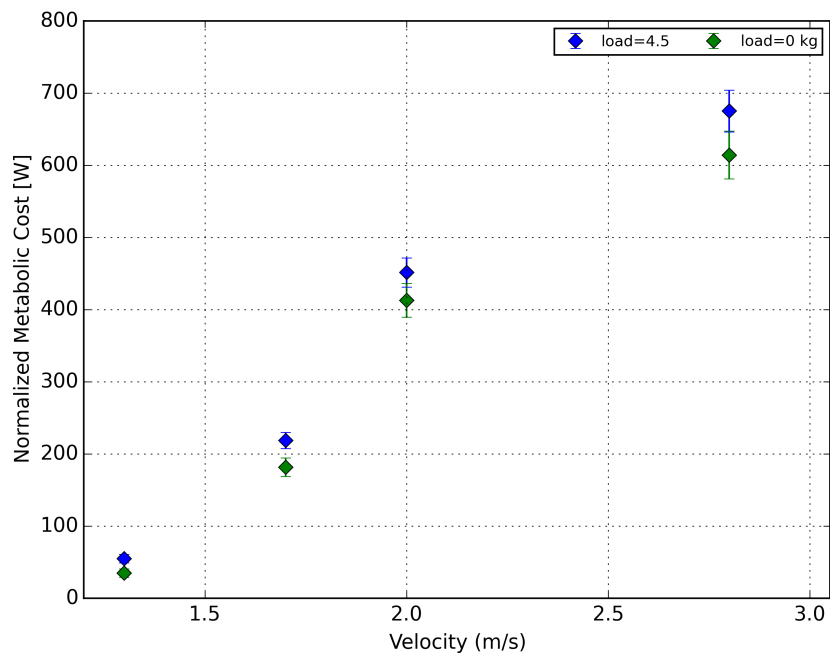
Figure 4.18: This graph depicts the difference between no load and a load of 4.5 kg placed on the upper shank. Each data point represents the mean across subjects, and the error bars represent the standard error of the mean. The metabolic cost is normalized by a slow walking baseline value (walking 1.0 m/s). This was done to normalize for variations in resting metabolic rate. Notice that the loaded condition cost grows faster than the unloaded condition. Ten subjects were tested at these conditions.

4.5.1 Expected Velocity Scaling

If we assume that the Power to Carry (defined in Eq. 4.5) is a continous and differentialble function, then the PC at a location L can be approximated by a Taylor series as:

$$PC_L(M,V) = P_L(M,V) - P_L(,0,V) = M\frac{\partial P_L(M,V)}{\partial M}|_{M=0} + H.O.T. \qquad (4.6)$$

Note that the higer order terms (H.O.T) can be ignored with small masses. This lets us focus on the linearized partial of added mass at a certain speed.

$$PC_L(M,V) \approx M \left.\frac{\partial P_L(M,V)}{\partial M}\right|_{M=0} \qquad (4.7)$$

The approximations of Eq. 4.7 imply that if an explicit equation for the incremental cost of carrying mass (either human or added mass) can be written, then an approximation of the PC can be derived. As it happens, Minetti [51] presented the energy per step to accelerate and deaccelerate limbs during locomtion as:

$$E_{step} = f_{stride}V^2(1 + (\frac{d}{1-d})^2)q. \qquad (4.8)$$

We can then convert this to Watts by mutiplying the forward velocity:

$$P = f_{stride}V^3(1 + (\frac{d}{1-d})^2)q. \qquad (4.9)$$

Using the fact that $V = \lambda f_{stride}$ we can replace the stride term to produce:

$$P = \frac{V^4}{\lambda}(1 + (\frac{d}{1-d})^2)q. \qquad (4.10)$$

where q is the mass geometry term for the human and added mass with no velocity dependency. This is written as:

$$q = (\pi^2/4)(a^2 + g^2)(m_l + b^2 m_u) \tag{4.11}$$

b length of the upper limb as a fraction of the lower limb

a fractional distance of the leg center of mass

g average radius of gyration of limbs, as a fraction of leg length

m_l mass of the lower limbs in kilograms

m_u mass of the upper limbs in kilograms

d ratio of stance time to stride time

Note that in this equation quanity of mass is isolated to m_l term and the placement of mass is isolated to the a and g term. As these two variables only affect the q term, we can easily take a partial derivative. Using our Taylor series approximation of PC in Eq. 4.7, the Power to Carry can be written as:

$$PC_L(M, V) \approx \underbrace{\frac{V^4}{\lambda}\left(1 + \left(\frac{d}{1-d}\right)^2\right)}_{\text{velocity terms}} \; \underbrace{\frac{\partial q}{\partial M} M}_{\text{mass terms}} \quad . \tag{4.12}$$

The mass term, $\frac{\partial q}{\partial M}$, was experimentally observed in Section 4.3. We experimentally observed that a linear approximation for the effect of mass was sufficient.

We believe the velocity term is dominated by the V^4 term. This is because step length is related to forward speed in walking by $v^{.42}$ [52]. For running the step length at running speeds can be approximated by small power of V as $1.03 + .37V$ [53]. Duty cycle is mainly influenced by the type of gait, staying in a range of 50-62% for walking, and 30% for running [51].

We would then expect scaling of the power to carry to be largely dominated by $\propto V^4$. Note that it was difficult to test for these high order terms as we had only four velocities, and the effect of gait made it questionable to treat walking and running in the same polynomial fit.

4.5.2   Midfoot Velocity Scaling

As the effect of added mass was most pronounced on the midfoot, we examined the non-linear scaling of the power to carry on midfoot. Note that as shown in Fig.4.19, a quartic and a linear function can plausibly explain the data. The low amount of variance of the velocities tested cause this limited resolution on the order of the polynomial.

We noticed that Franz and Kram [54] had conducted studies on the effect of added mass at running speeds of 3.35 m/s. While their study was interested in comparing the difference types of shoe, they did test subjects with lead weights placed on the top of the midfoot. The weights ranged from 0.3 kg to 0.8 kg of bilateral load. Franz and Kram measured a metabolic effect of 60.3 W/kg of bilateral load on the midfoot. This seems to imply that power to carry scales linearly with velocity.
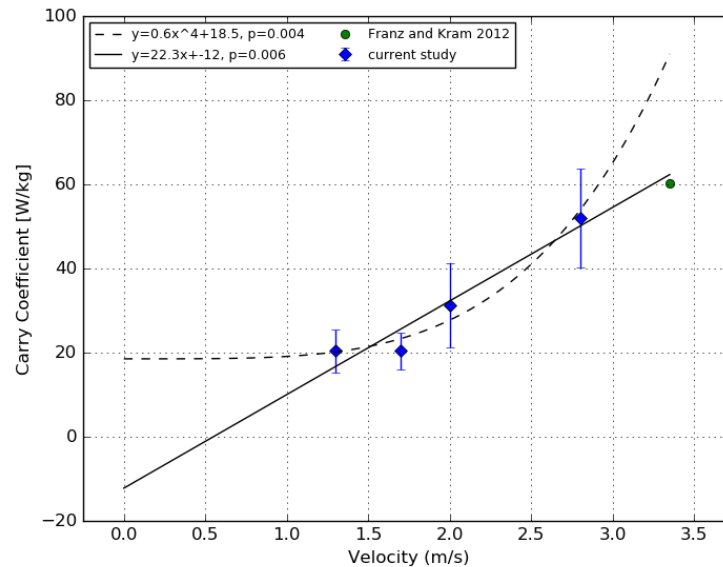

Figure 4.19: This graphs shows the Power to Carry at the midfoot [W] divided by the load tested [kg]. This give a coarse approximation of the coefficients shown in Table 4.3. Note that both a linear trend line (p = .006) and a quartic function (p = .004) could explain the data that we observed. When we extrapolate the linear function, it more closely agrees with the experimental data observed by Franz and Kram [54]. In contrast, the quartic fit extrapolation does not match the published literature.

4.5.3 Planar Fit

$$PC_L = \alpha_L MV$$

Because the previous section implied that it was likely that the effect of added mass would scale linearly with velocity, we tested planar fits on the data. Note that a statistical difference was found between the foot and midfoot coefficients (p = .0002). This implies that an ankle actuator that places more mass on the shank will be less burdensome. There was no statistical difference between the upper shank and the lower thigh (p = .87). This implies that in the design of an actuator localized at the knee, we can place weight above or below the joint with little consequence to the metabolics.

Location	α_L [W/(kg*m/s)]
midfoot	17.58 ± 2.07
lower shank	9.2449 ± 1.366
upper shank	4.4544 ± 0.752
lower thigh	4.61644 ± 0.532

Table 4.4: Best fit planes for $PC_L = \alpha_L MV$. No statistical difference was found between the upper shank and the lower thigh (p = .87)
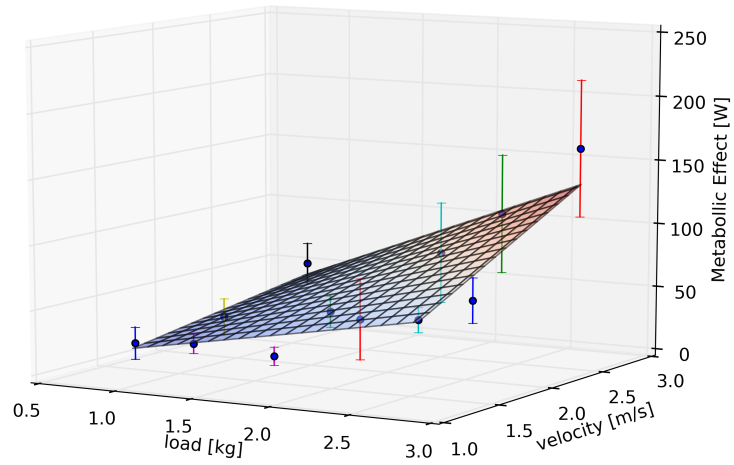
Figure 4.20: This depicts ordinary least squares fit on the data at the midfoot. The best fit is $PC = 17.58 * M * V$ (p = 7.88e-12). The standard error on the coefficient is 2.07.
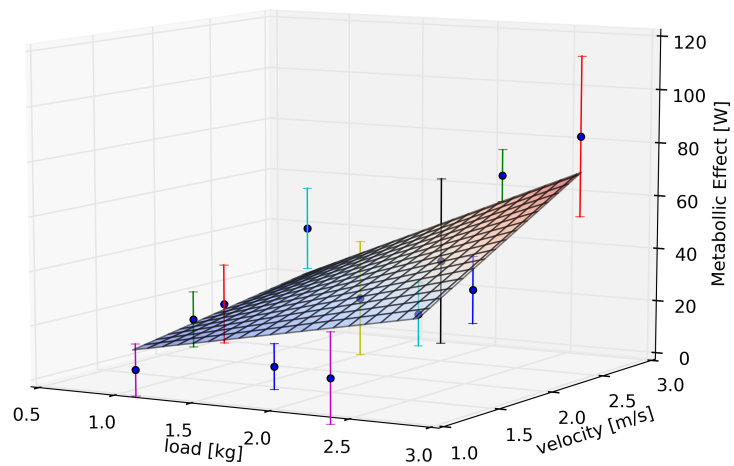

Figure 4.21: This depicts ordinary least squares fit on the data at the lower shank. The best fit is $PC = 9.2449 * M * V$ (p = 5.76e-10). The standard error on the coefficient is 1.366.

97
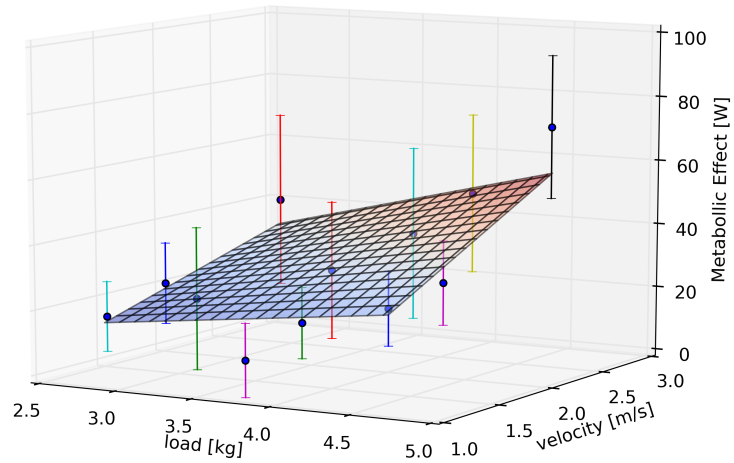
Figure 4.22: This depicts ordinary least squares fit on the data at the upper shank. The best fit is $PC = 4.4544 * M * V$ (p = 3.20e-08). The standard error on the coefficient is 0.752.
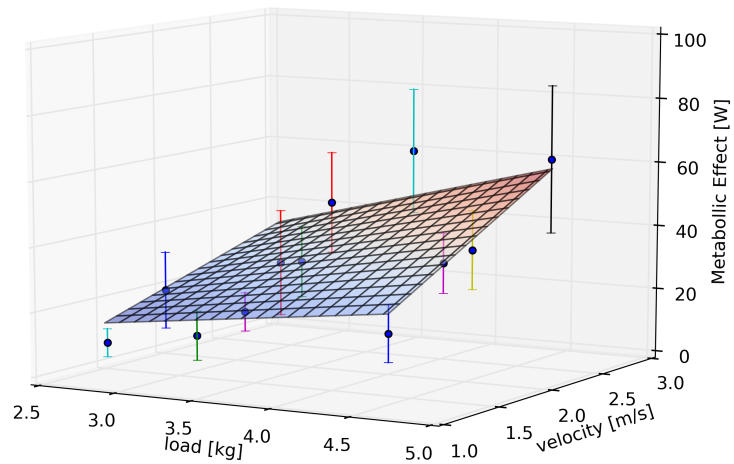

Figure 4.23: This depicts ordinary least squares fit on the data at the upper shank. The best fit is $PC = 4.61644 * M * V$ (p = 6.17e-14). The standard error on coefficient is 0.532.
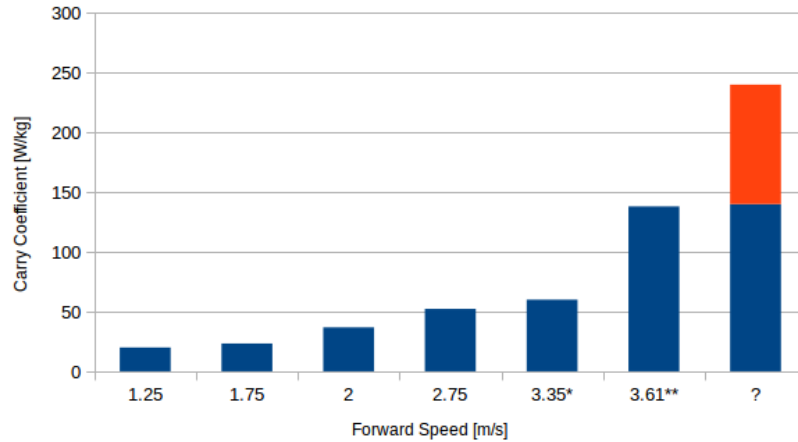
4.5.4   Added Mass Conclusions

Figure 4.24: This graph compares the carry coefficient (Watts of effect per kilogram of orthosis) at the midfoot for our study and related studies. Note that when we augment the trend of increasing burden with forward speed, it is further supported by literature in the field. Note that these studies utilized small mass (0.2 kg bilateral load) and well-trained runners to keep the metabolic data in the aerobic regime. The far right bar represents the speed at which it is not possible to maintain aerobic energy expenditure. While our respired gasses can estimate a portion of the cost (blue), there is an unknown amount (red) that is creating lactic acid and not immediately apparent in the respired gasses. * Represents data from Franz et al.[54]. ** Represents data from Divert et al.[55].

This experiment strongly implies that the power to carry increases with forward velocity at all locations. There was not enough statistical power to determine a polynomial fit to the data. As can be seen in Fig.4.24, there is substantial literature supporting large increases in the metabolic burden of mass at the foot. There is a lack of research determining the effect at locations such as the shank and the thigh, but our data implies that a similar increasing trend may exist as well. Our data does show that the distal mass sensistivity is very high at the lower shank and the foot. Exoskeleton designers should optimize weight placements to as proximal as design constraints allow. The sensitivity of metabolic burden to location appears to decrease for weights placed around the knee. Our study did not find a significant difference between mass placed slightly above or

slightly below the knee.

Future work will be aimed at determining the exact polynomial fit for the effect of mass. For this experiment we plan on testing one location and one mass across 10 subjects. We will then randomly select velocities uniformily between 0.25 m/s and 2.25 m/s walking. The categorical nature of the previous mass study was useful for conducting statistical tests, but it limited our ability to conduct regressions with velocity. A polynomial regression is best done with a continous variance so that information is attained from regions, not select points.

4.6   Added Power Pilot

Figure 4.25: The Otherlab exoskeleton utilizes cloth pneumatic actuators for toeoff. This novel cloth actuator functions equivalently to a pneumatic expansion cylinder, but with much lower added weight.

For the benefit of added power, we have studied three subjects with varying power levels at running and walking speeds. The exoskeleton delivers high-peak powers at the ankle (Refer to Fig. 4.25). Currently, we are power limited by hardware reliability as we continue to bring the up to higher operating powers. Given planned structural upgrades to the design, we anticipate additional data will confirm preliminary results, demonstrating the first reported metabolic benefit by an exoskeleton operating at high mechanical power levels.

With regard to assistive power, Mooney et al. suggest power has a linear effect on the metabolic burden; however, a simple thought experiment leads to the hypothesis that there is a point where you begin to see diminishing returns from adding power to the operator. For a given design, extremely low levels of assistance in power result in a metabolic burden because not enough power is to overcome the mass of the device.

Similarly, if too much power is introduced to the leg, we reach a point where the assistance disrupts the operator's natural biomechanics. This may create a metabolic burden at high levels of assistance. In between, there is an ideal amount of added mechanical power that the operator can accept and leverage without disrupting his or her biomechanics. This hypothesized shape is depicted by the green dashed line in Fig. 4.26. We suspect that diminishing returns have not yet been observed because all published beneficial exoskeletons have output less than 30 W at the ankle [47]. We plan to expand the observed human responses to 100 W of mechanical powers.

4.6.1   Preliminary Results

Efficiency of Positive Mechanical Power

Our preliminary data corresponds to an ankle joint muscle-tendon "apparent efficiency" [47] of $\eta^{+}_{ankle} = .30$ (mechanical W per metabolic W) at 2.75 m/s running for the lower power range, where $\eta^{+}_{ankle} = \frac{Average\ exoskeleton\ positive\ mechanical\ power}{\Delta\ Net\ human\ metabolic\ power}$. Note that Farris et. al. [56] report an overall positive work efficiency of .39 $\frac{MechW}{MetabolicW}$. The value we measured of .29 is not statistically significantly different (p = .35).
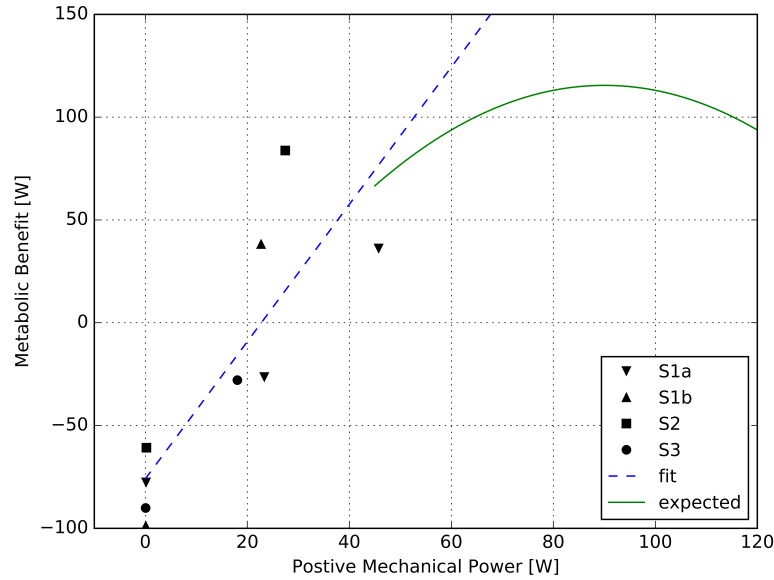
Figure 4.26: Individual responses to positive mechanical power supplied by (and added mass of) an exoskeleton. On average these subjects used 1100 W to run unassisted at 2.8 m/s. All data were taken from subjects running at 2.8 m/s. There were 9 tests distributed across 3 subjects (S1,S2,S3). A least squares interpolation yields $y = 3.34x - 75.9$ with $R^2 = 0.71$ (p = .0043). This implies we will create the first exoskeleton to produce a metabolic benefit while the user is running. Note that the green dashed line illustrates hypothetical diminishing returns that we suspect will likely occur at unknown higher power levels.

Power to Carry

Note that with three subjects, we were able to estimate the power to carry of our exoskeleton. The bilateral mass placed on the lower shank is 1 kg, and the bilateral mass on the midfoot is 1 kg. As can be seen in Table 4.3, the effect on midfoot at running speeds is 53.2 W/kg, and the effect on the lower shank is 27.7 W/kg. Our mass study predicted a metabolic burden of 80.9 W. Our least squares regression estimated a burden of 75.9 ± 17.4 W when tested across three subjects. Our prediction was not statistically different from what our regression measured (p = .79).
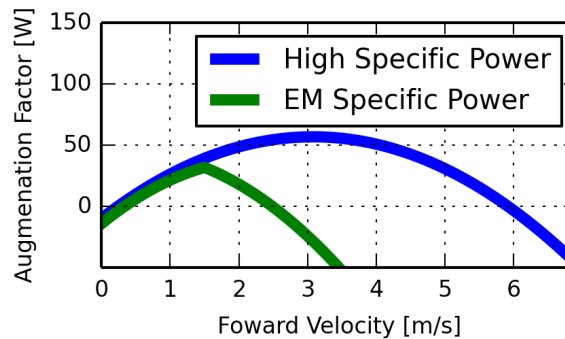
4.7 Augmentation Factor Conclusions

Figure 4.27: This figures compares two devices of the same mass, but different power capacities. The high specific power can deliver more power for the same mass and as a result can be useful over a larger range of speeds. In contrast, a electromechanical (EM) device can only offset its mass burden at slow walking speeds. The corner in the green curve comes from the power saturation. At this point the mass burden grows, but the power supplied by the device remains static. Refer to Fig 4.15 and Fig 4.19 for more details on mass burden with speed.

Our recent experimental data indicate that we have made the first metabolically beneficial powered running exoskeleton. With additional simulation data, we aim to explain why our device succeeds where so many others have failed. Although we hope our simulations will explain experimental data presented here, whether theory agrees

with or contradicts our experiments to date will be an interesting, publishable result, given the significance of the existing, unpublished experimental data itself.

Also, our analysis is structured to expand and correct the augmentation factor equation. With a revised equation, we can quantitatively understand how to balance the power and mass of an exoskeleton. This understanding will allow exoskeleton designers to optimize performance more effectively, minimizing the arduous prototype and test cycle. The central dilemma to an exoskeleton mechanical design is weighing the added power and the burden of added weight. This dilemma is captured succinctly with one attribute: the specic power of the actuation architecture being used. To demonstrate this, consider an example design similar to that in Mooney et al. [11] that is a single ankle design sized to provide around 25 W of positive mechanical power to maximize benefit for a 1.5 m/s walk (refer to Fig. 4.27).

This single design necessarily has a fixed mass across all velocities. It design creates two limits: at velocities less than the design velocity (1.5 m/s) the augmentation factor is limited by how much power the operator can accept, while at higher velocities the augmentation factor is limited by the peak power of the actuator. These two limits result in a peak achievable augmentation factor and a dened range of velocities where the device can provide metabolic neutrality or better. In contrast, a high specic power alternative with a comparable mass but a significantly increased peak power capacity can greatly increase the available augmentation capability. As a result, the recent push towards lightweight exoskeletons has been somewhat misguided. Achieving high augmentation factors across a wide range of velocities cannot be done solely by focusing on reducing weight of a design; a more essential aspect is to provide actuation with higher specic powers– more power with less weight.

Chapter 5

Conclusion

In the first technical Chapter 2 is on dynamic coupling between planes. We showed how coupling can provide a stable, energy efficient, and agile extension to 3D stabilization. Our analysis showed that the non-linear roll dynamics appear to be central to coupling between planes. Unexpectedly, this technique of stabilization worked across a variety of step timing and step lengths. Finally, we showed that the analysis of sagittal constrained walker held true as a course approximation for a full 3D simulation. This is valuable in that we can press forward with investigations of the sagittal system, and have confidence that the analysis holds for full 3D systems.

With the confidence that the sagittal model captures the salient features of walking, we returned in Chapter 3 to the sagittal 5 link walker. The challenge with under actuated dynamic walkers had been controlling foothold selection. We were able to surmount this hurdle by using a simple switching policy. We were able to identify important connectivity and distribution properties of the mesh to solving the foothold selection and avoidance problems. This work has been extended by the group and shows the ability to be applied to a various types of robots [40].

To balance the simulation and theoretical nature of these chapters, we presented experimental data with Chapter 4. We approached the human as a highly energy optimized robot and studied the effect of adding mass to the person. This has implications

on how the human muscular mass was optimized for extremely efficient legged locomotion. The information of added mass and power can be used to create new generation of extremely effective metabolically beneficial exoskeletons. The preliminary testing has shown metabolic benefits at walking and running speeds for single subjects.

Bibliography

[1] S. H. Collins, M. Wisse, and A. Ruina, *A three-dimensional passive-dynamic walking robot with two legs and knees*, *The International Journal of Robotics Research* **20** (2001), no. 7 607–615.

[2] T. McGeer, *Passive dynamic walking*, *the international journal of robotics research* **9** (1990), no. 2 62–82.

[3] A. D. Kuo, *Choosing your steps carefully*, *Robotics & Automation Magazine, IEEE* **14** (2007), no. 2 18–29.

[4] R. Margaria, *Positive and negative work performances and their efficiencies in human locomotion*, *Internationale Zeitschrift für angewandte Physiologie einschließlich Arbeitsphysiologie* **25** (1968), no. 4 339–351.

[5] P. A. Bhounsule, J. Cortell, A. Grewal, B. Hendriksen, J. D. Karssen, C. Paul, and A. Ruina, *Low-bandwidth reflex-based control for lower power walking: 65 km on a single battery charge*, *The International Journal of Robotics Research* **33** (2014), no. 10 1305–1321.

[6] H. A. Quintero, R. J. Farris, and M. Goldfarb, *Control and implementation of a powered lower limb orthosis to aid walking in paraplegic individuals*, in *Rehabilitation Robotics (ICORR), 2011 IEEE International Conference on*, pp. 1–6, IEEE, 2011.

[7] L. Martin, "Hulc.." `http://www.lockheedmartin.com/us/products/hulc.html`.

[8] Raytheon, "XOS2."

[9] K. Amundson, *Human Exoskeleton Control and Energetics*. PhD thesis, UC Berkeley, Berkeley, CA, USA, 2007.

[10] M. Wehner, B. Quinlivan, P. M. Aubin, E. Martinez-Villalpando, M. Baumann, L. Stirling, K. Holt, R. Wood, and C. Walsh, *A lightweight soft exosuit for gait assistance*, in *Robotics and Automation (ICRA), 2013 IEEE International Conference on*, pp. 3362–3369, IEEE, 2013.

[11] L. M. Mooney, E. J. Rouse, and H. M. Herr, *Autonomous exoskeleton reduces metabolic cost of human walking during load carriage*, Journal of neuroengineering and rehabilitation **11** (2014), no. 1 1.

[12] C. O. Saglam and K. Byl, *Stability and gait transition of the five-link biped on stochastically rough terrain using a discrete set of sliding mode controllers*, in *Robotics and Automation (ICRA), 2013 IEEE International Conference on*, pp. 5675–5682, IEEE, 2013.

[13] C. O. Saglam and K. Byl, *Switching policies for metastable walking*, in *Decision and Control (CDC), 2013 IEEE 52nd Annual Conference on*, pp. 977–983, IEEE, 2013.

[14] C. E. Bauby and A. D. Kuo, *Active control of lateral balance in human walking*, Journal of biomechanics **33** (2000), no. 11 1433–1440.

[15] N. Matsusaka, *Control of the medial-lateral balance in walking*, Acta Orthopaedica **57** (1986), no. 6 555–559.

[16] D. A. Winter, *Human balance and posture control during standing and walking*, Gait & posture **3** (1995), no. 4 193–214.

[17] D. A. Winter, F. Prince, J. Frank, C. Powell, and K. F. Zabjek, *Unified theory regarding a/p and m/l balance in quiet stance*, Journal of neurophysiology **75** (1996), no. 6 2334–2343.

[18] C. D. MacKinnon and D. A. Winter, *Control of whole body balance in the frontal plane during human walking*, Journal of biomechanics **26** (1993), no. 6 633–644.

[19] M. Wisse, *Three additions to passive dynamic walking: actuation, an upper body, and 3d stability*, International Journal of Humanoid Robotics **2** (2005), no. 04 459–478.

[20] M. Wisse and A. L. Schwab, *Skateboards, bicycles, and three-dimensional biped walking machines: velocity-dependent stability by means of lean-to-yaw coupling*, The International Journal of Robotics Research **24** (2005), no. 6 417–429.

[21] B. Bechstein, *Improvements in and relating to toys*, UK Patent (1912), no. 7453.

[22] R. Tedrake, T. W. Zhang, M.-f. Fong, and H. S. Seung, *Actuating a simple 3d passive dynamic walker*, in *Robotics and Automation, 2004. Proceedings. ICRA'04. 2004 IEEE International Conference on*, vol. 5, pp. 4656–4661, IEEE, 2004.

[23] C. O. Saglam and K. Byl, *Quantifying the trade-offs between stability versus energy use for underactuated biped walking*, in *Intelligent Robots and Systems (IROS 2014), 2014 IEEE/RSJ International Conference on*, pp. 2550–2557, IEEE, 2014.

[24] D. G. Hobbelen and M. Wisse, *Limit cycle walking.* I-Tech Education and Publishing, Vienna, Austria, 2007.

[25] E. Todorov, T. Erez, and Y. Tassa, *Mujoco: A physics engine for model-based control*, in *IEEE Int. Conf. on Intel. Robots and Systems (IROS)*, pp. 5026–5033, 2012.

[26] E. R. Westervelt, J. W. Grizzle, C. Chevallereau, J. H. Choi, and B. Morris, *Feedback control of dynamic bipedal robot locomotion*, vol. 28. CRC press, 2007.

[27] C. O. Saglam and K. Byl, *Quantifying and optimizing stability of bipedal walking gaits*, in *IEEE International Conference on Robotics and Automation (ICRA)*, 2015. submitted.

[28] M.-Y. Chen and K. Byl, *Analysis and control techniques for the compass gait with a torso walking on stochastically rough terrain*, in *American Control Conference (ACC), 2012*, pp. 3451–3458, IEEE, 2012.

[29] J. D. Ortega and C. T. Farley, *Individual limb work does not explain the greater metabolic cost of walking in elderly adults*, *Journal of applied physiology* **102** (2007), no. 6 2266–2273.

[30] C. O. Saglam and K. Byl, *Robust policies via meshing for metastable rough terrain walking*, RSS, 2014.

[31] M. Vukobratović and B. Borovac, *Zero-moment pointthirty five years of its life*, *International Journal of Humanoid Robotics* **1** (2004), no. 01 157–173.

[32] A. Goswami, *Postural stability of biped robots and the foot-rotation indicator (fri) point*, *The International Journal of Robotics Research* **18** (1999), no. 6 523–533.

[33] E. R. Westervelt, J. W. Grizzle, and D. E. Koditschek, *Hybrid zero dynamics of planar biped walkers*, *Automatic Control, IEEE Transactions on* **48** (2003), no. 1 42–56.

[34] T. Yang, E. Westervelt, A. Serrani, and J. P. Schmiedeler, *A framework for the control of stable aperiodic walking in underactuated planar bipeds*, *Autonomous Robots* **27** (2009), no. 3 277–290.

[35] H.-W. Park, A. Ramezani, and J. Grizzle, *A finite-state machine for accommodating unexpected large ground-height variations in bipedal robot walking*, *Robotics, IEEE Transactions on* **29** (2013), no. 2 331–345.

[36] C. O. Saglam and K. Byl, *Meshing hybrid zero dynamics for rough terrain walking*, ICRA 2015.

[37] J. S. Matthis and B. R. Fajen, *Humans exploit the biomechanics of bipedal gait during visually guided walking over complex terrain*, Proceedings of the Royal Society B: Biological Sciences **280** (2013), no. 1762 20130700.

[38] R. D. Gregg, A. K. Tilton, S. Candido, T. Bretl, and M. W. Spong, *Control and planning of 3-d dynamic walking with asymptotically stable gait primitives*, Robotics, IEEE Transactions on **28** (2012), no. 6 1415–1423.

[39] S. E. Sovero, C. O. Saglam, and K. Byl, *Passive frontal plane stabilization in 3d walking*, Submitted to IROS 2015.

[40] V. Paris, T. Strizic, J. Pusey, and K. Byl, *Tools for the design of stable yet nonsteady bounding control*, in *American Control Conference (ACC), 2016*, IEEE, 2016.

[41] Maksim, "Scc.png." webpage, March, 2006. GNU Free Documentation License.

[42] R. Bellman, *A markovian decision process*, tech. rep., DTIC Document, 1957.

[43] G. S. Sawicki and D. P. Ferris, *Powered ankle exoskeletons reveal the metabolic cost of plantar flexor mechanical work during walking with longer steps at constant step frequency*, Journal of Experimental Biology **212** (2009), no. 1 21–31.

[44] P. Malcolm, W. Derave, S. Galle, and D. De Clercq, *A simple exoskeleton that assists plantarflexion can reduce the metabolic cost of human walking*, PloS one **8** (2013), no. 2 e56137.

[45] R. C. Browning, J. R. Modica, R. Kram, A. Goswami, *et. al.*, *The effects of adding mass to the legs on the energetics and biomechanics of walking*, Medicine and science in sports and exercise **39** (2007), no. 3 515.

[46] G. S. Sawicki and D. P. Ferris, *Mechanics and energetics of level walking with powered ankle exoskeletons*, Journal of Experimental Biology **211** (2008), no. 9 1402–1413.

[47] G. S. Sawicki and D. P. Ferris, *Mechanics and energetics of incline walking with robotic ankle exoskeletons*, Journal of Experimental Biology **212** (2009), no. 1 32–41.

[48] S. H. Collins, M. B. Wiggin, and G. S. Sawicki, *Reducing the energy cost of human walking using an unpowered exoskeleton*, Nature **522** (2015), no. 7555 212–215.

[49] S. J. Mattes, P. E. Martin, and T. D. Royer, *Walking symmetry and energy cost in persons with unilateral transtibial amputations: matching prosthetic and intact limb inertial properties*, Archives of physical medicine and rehabilitation **81** (2000), no. 5 561–568.

[50] P. De Leva, *Adjustments to zatsiorsky-seluyanov's segment inertia parameters*, *Journal of biomechanics* **29** (1996), no. 9 1223–1230.

[51] A. E. Minetti, *A model equation for the prediction of mechanical internal work of terrestrial locomotion*, *Journal of biomechanics* **31** (1998), no. 5 463–468.

[52] J. E. Bertram and A. Ruina, *Multiple walking speed–frequency relations are predicted by constrained optimization*, *Journal of theoretical Biology* **209** (2001), no. 4 445–453.

[53] P. G. Weyand, D. B. Sternlight, M. J. Bellizzi, and S. Wright, *Faster top running speeds are achieved with greater ground forces not more rapid leg movements*, *Journal of applied physiology* **89** (2000), no. 5 1991–1999.

[54] J. R. Franz, C. M. Wierzbinski, and R. Kram, *Metabolic cost of running barefoot versus shod: is lighter better*, *Med Sci Sports Exerc* **44** (2012), no. 8 1519–1525. shoe runnning metabolic.

[55] C. Divert, G. Mornieux, P. Freychat, L. Baly, F. Mayer, and A. Belli, *Barefoot-shod running differences: shoe or mass effect?*, *International journal of sports medicine* **29** (2008), no. 6 512–518.

[56] D. J. Farris and G. S. Sawicki, *The mechanics and energetics of human walking and running: a joint level perspective*, *Journal of The Royal Society Interface* (2011) rsif20110182. Useful metabollics, joint torque and powers for walking and running.